Gut microbiome dysbiosis during COVID-19 is associated with increased risk for bacteremia and microbial translocation.

Mericien Venzon[*1,2], Lucie Bernard-Raichon[*2], Jon Klein[*3], Jordan E. Axelrad[*4], Chenzhen Zhang[*5], Grant A. Hussey[5], Alexis P. Sullivan[5], Arnau Casanovas-Massana[6], Maria G. Noval[7], Ana M. Valero-Jimenez[7], Juan Gago[1,8], Gregory Putzel[7,12], Alejandro Pironti[7,12], Evan Wilder[4], Yale IMPACT Research Team[11], Lorna E. Thorpe[8,12], Dan R. Littman[2,9], Meike Dittmann[7], Kenneth A. Stapleford[7], Bo Shopsin[7,10,12], Victor J. Torres[7,12], Albert I. Ko[6], Akiko Iwasaki[3,9], Ken Cadwell[2,4,7,12]†, Jonas Schluter[5,7,12]†

1. Vilcek Institute of Graduate Biomedical Sciences, New York University Grossman School of Medicine, New York, NY, USA
2. Kimmel Center for Biology and Medicine at the Skirball Institute, New York University Grossman School of Medicine, New York, NY, USA
3. Department of Immunobiology, Yale University School of Medicine, New Haven, CT, USA
4. Division of Gastroenterology, Department of Medicine, New York University Grossman School of Medicine, New York, NY, USA
5. Institute for Systems Genetics, New York University Grossman School of Medicine, New York, NY, USA
6. Department of Epidemiology of Microbial Diseases, Yale School of Public Health, New Haven, CT, USA.
7. Department of Microbiology, New York University Grossman School of Medicine, New York, NY, USA
8. Department of Population Health, New York University Grossman School of Medicine, New York, NY, USA.
9. Howard Hughes Medical Institute, Chevy Chase, MD.
10. Department of Medicine, Division of Infectious Diseases, New York University Grossman School of Medicine, New York, NY, USA
11. IMPACT team members listed in the appendix.
12. Antimicrobial-Resistant Pathogens Program, New York University School of Medicine, New York, NY, USA.

*) These authors contributed equally

Correspondence:

† ken.cadwell@nyulangone.org

† jonas.schluter@nyulangone.org

Abstract

The microbial populations in the gut microbiome have recently been associated with COVID-19 disease severity. However, a causal impact of the gut microbiome on COVID-19 patient health has not been established. Here we provide evidence that gut microbiome dysbiosis is associated with translocation of bacteria into the blood during COVID-19, causing life-threatening secondary infections. Antibiotics and other treatments during COVID-19 can potentially confound microbiome associations. We therefore first demonstrate in a mouse model that SARS-CoV-2 infection can induce gut microbiome dysbiosis, which correlated with alterations to Paneth cells and goblet cells, and markers of barrier permeability. Comparison with stool samples collected from 96 COVID-19 patients at two different clinical sites also revealed substantial gut microbiome dysbiosis, paralleling our observations in the animal model. Specifically, we observed blooms of opportunistic pathogenic bacterial genera known to include antimicrobial-resistant species in hospitalized COVID-19 patients. Analysis of blood culture results testing for secondary microbial bloodstream infections with paired microbiome data obtained from these patients indicates that bacteria may translocate from the gut into the systemic circulation of COVID-19 patients. These results are consistent with a direct role for gut microbiome dysbiosis in enabling dangerous secondary infections during COVID-19.

52 **Main text**

53 A better understanding of factors contributing to the pathology of coronavirus disease 2019
54 (COVID-19) is an urgent global priority. Previous reports have demonstrated that severe
55 COVID-19 is frequently associated with specific inflammatory immune phenotypes,
56 lymphopenia, and a generally disproportionate immune response leading to systemic organ
57 failure[1,2]. Even in mild cases, gastrointestinal symptoms are reported frequently, and recent
58 studies reported that COVID-19 patients lose commensal taxa of the gut microbiome during
59 hospitalization[3–5]. Differences in gut bacterial populations relative to healthy controls were
60 observed in all COVID-19 patients, but most strongly in patients who were treated with
61 antibiotics during their hospitalization[4]. Most recently, COVID-19 patients treated with broad
62 spectrum antibiotics at admission were shown to have increased susceptibility to multi-drug
63 resistant infections and nearly double the mortality rate from septic shock[6,7]. Furthermore,
64 although initially estimated to be low (6.5%)[8], more recent studies have detected bacterial
65 secondary infections in as much as 12-14% of COVID-19 patients[9,10]. However, the causal
66 direction of the relationship between disease symptoms and gut bacterial populations is not yet
67 clear.

68 Complex gut microbiota ecosystems can prevent the invasion of potentially pathogenic
69 bacteria[11,12]. Conversely, when the gut microbiota incurs damage, such as through antibiotics
70 treatment, competitive exclusion of pathogens is weakened[13–15] and potentially dangerous
71 blooms of antibiotic resistant bacterial strains can occur[16,17]. In immunocompromised cancer
72 patients, blooms of Enterococcaceae and Gram-negative proteobacteria can lead to gut
73 dominations by few or single species[18–21]. Such gut domination events are dangerous to these
74 patients because they are associated with increased risk of translocation of antibiotic resistant
75 bacteria from the gut into the blood stream[18]. Bacterial co-infection can also cause life-
76 threatening complications in patients with severe viral infections[7,8,22]; therefore, antibacterial
77 agents were administered empirically to nearly all critically ill suspected COVID-19 patients
78 since the incidence of bacterial superinfection was unknown early during the pandemic[4,23].
79 However, it is now known that nosocomial infection during prolonged hospitalization is the
80 primary threat to patients with COVID-19[24], rather than bacterial co-infection upon hospital
81 admission[9,25–27]. Evidence from immunocompromised cancer patients suggests that
82 indiscriminate administration of broad-spectrum antibiotics may, counter-intuitively, increase

83 nosocomial bloodstream infection (nBSI) rates by causing gut dominations of resistant microbes
84 that can translocate into the blood[18,28]. Thus, empiric antimicrobial use, i.e. without direct
85 evidence for a bacterial infection, in patients with severe COVID-19 may be especially
86 pernicious because it may select for antimicrobial resistance and could promote gut
87 translocation-associated nBSI.

88 The role of the gut microbiome in respiratory viral infections in general[29–31], and in
89 COVID-19 patients in particular, is only beginning to be understood. Animal models of
90 influenza virus infection have uncovered mechanisms by which the microbiome influences
91 antiviral immunity[32–34], and in turn, the viral infection was shown to disrupt the intestinal barrier
92 of mice by damaging the gut microbiota[35,36]. Hence, we hypothesized that gut dysbiosis during
93 COVID-19 may be associated with BSIs. To test this, we first determined whether SARS-CoV-2
94 infection could directly cause gut dysbiosis independently of hospitalization and treatment. K18-
95 hACE2 mice (*K18-ACE2tg* mice), express human *ACE2* driven by the *cytokeratin-18* promoter
96 (*K18-ACE2tg* mice). Although the overexpression of ACE2 prevents investigation of long term
97 consequences of infection due to potential non-specific disease, which is a major limitation of
98 the model, an advantage of these mice is that they develop severe respiratory disease in a virus
99 dose-dependent manner, partially mirroring what is observed in COVID-19 patients[37–40]. Daily
100 changes in fecal bacterial populations were monitored following intranasal inoculation of mice
101 with a range of doses (10, 100, 1000, and 10000 PFU) of SARS-CoV-2 or mock-treatment (**Fig.
102 1a, Extended Data Fig. S1**). Although we detected viral RNA in the lungs of mice infected
103 with doses as low as 100 PFU (**Extended Data Fig. S1c**), mice inoculated with doses lower than
104 10000 PFU displayed minimal or no signs of disease (**Extended Data Fig. S1a,b**), and as
105 expected based on this outcome, shifts in their microbiome were inconsistent (**Extended Data
106 Fig. S2**). Thus, we focused on findings from the 10000 PFU inoculum.

107 Mice infected with 10000 PFU displayed weight loss and other signs of disease around
108 day 4 (**Extended Data Fig. S1a,b, S2e,f**), alongside microbiome changes characterized by a
109 significant loss of alpha diversity (inverse Simpson index, **Fig. 1b**) corresponding to shifts in the
110 bacterial community composition (**Fig. 1c,d**). We performed time series analyses on bacterial
111 family abundances, contrasting their trajectories in infected (10000 PFU) and uninfected mice.
112 This revealed that the strongest shift over time in infected mice was characterized by significant
113 increases of Akkermansiaceae ($p<0.0002$, **Fig. 1d**). Ranking all bacterial family trajectories by

114 their estimated changes over time in infected mice showed that this increase in Akkermansiaceae
115 was accompanied by significant losses of Clostridiaceae 1, a family of obligate anaerobe
116 bacteria, and of Erysipelotrichiaceae (**Fig. 1e**). These results demonstrated that SARS-CoV-2
117 infection leads to gut microbiome dysbiosis over time in a mouse model.
118 We then determined if this dysbiosis was also associated with intestinal defects that could
119 enable translocation of bacteria into the blood. While several of the infected mice displayed signs
120 of barrier dysfunction the observed differences in plasma concentrations of Fluorescein
121 isothiocyanate (FITC)-dextran following its administration by gavage, or other markers of
122 intestinal barrier permeability, fatty acid-binding protein (iFABP), Lipopolysaccharide-binding
123 protein (LBP), and citrulline did not reach significance (**Extended Data Fig. S3a,b**). The
124 reduced colon lengths as well as reductions in the villus lengths in the duodenum or ileum, i.e.
125 markers of overt inflammation, that we observed were also non-significant compared with
126 control mice (**Extended Data Fig. S3c,d**). However, infected mice that had incurred the most
127 severe microbiome injury in the form of diversity loss showed the most evidence of gut
128 permeability–the highest FITC-dextran concentrations in the blood of mice detected across all
129 samples came from the two out of the four mice with the most extreme dysbiosis and highest
130 levels of Akkermansiaceae, a family of mucin-degrading bacterial species (**Extended Data Fig.
131 S4)**.
132 Interestingly, we also detected a significant increase in the number of mucus-producing
133 goblet cells and a decrease in the number of Paneth cells in the ileum (but not in the duodenum)
134 of infected mice (**Fig. 2a,c and Extended Data Fig. S3e**). The decrease in Paneth cells was
135 accompanied by structural abnormalities, most notably deformed or misplaced granules (**Fig.
136 2b**). These morphological abnormalities in Paneth cells were reminiscent of observations in the
137 ileum of patients with inflammatory bowel disease (IBD) as well as in a virally-triggered animal
138 model of IBD, where such structures were indicative of defects in packaging and secretion of the
139 granule protein lysozyme[41–43]. Thus, to quantify the Paneth cell granule defect, we performed
140 lysozyme immunofluorescence and found a significant increase in the proportion of Paneth cells
141 displaying abnormal staining patterns compared with the controls (**Fig. 2b,c**). We then
142 investigated if these physiological defects were associated with dysbiosis in the microbiome. The
143 most severely sick mice also had the most striking shifts in their microbiome composition and
144 the lowest microbiota diversity at the end of the experiment (**Extended Data Fig. S4a,b**). To

145 associate the observed physiological defects with microbiome dysbiosis, we plotted the numbers
146 of goblet cells per crypt-villus unit and Paneth cells per crypt, as well as the percentage of
147 abnormal Paneth cells against bacterial alpha diversity and the $\log_{10}$-relative abundance of
148 Akkermansiaceae (**Fig. 2d,e**). Goblet cell counts per crypt-villus unit were negatively correlated
149 with alpha diversity, and, conversely, positively correlated with Akkermansiaceae. While no
150 statistically significant association was found between diversity, Akkermansiaceae abundance
151 and Paneth cell counts per crypt, we observed a striking positive correlation between the
152 percentage of abnormal Paneth cells and Akkermansiaceae, and a corresponding negative
153 correlation with diversity. We were unable to reliably detect viral RNA in intestinal samples
154 (**Extended Data Fig. S1c**), raising the possibility that systemic immune responses rather than
155 direct cytotoxicity from local viral infection mediate these changes. Altogether, these results
156 show that the gut microbiome dysbiosis observed in K18-hACE2 mice infected with a high dose
157 of SARS-CoV-2 are associated with alterations in key epithelial cells, and signs of barrier
158 permeability in the mice displaying the greatest disruption in microbiome diversity.
159 To investigate the microbiome in COVID-19 patients, we profiled the bacterial
160 composition of the fecal microbiome in 130 samples (**Fig. 3a**) obtained from SARS-CoV-2
161 infected patients treated at NYU Langone Health (NYU, 67 samples from 60 patients) and Yale
162 New Haven Hospital (YALE, 63 samples from 36 patients, **Supplementary Table 1**). Analysis
163 of metagenomic data obtained from sequencing of the 16S rRNA genes revealed a wide range of
164 bacterial community diversities, as measured by the inverse Simpson index, in samples from
165 both centers (NYU: [1.0, 32.3], YALE: [1.5, 29.3], **Fig. 3b**); on average, samples from NYU
166 were less diverse (-4, $p<0.01$, two-tailed T-test, **Fig. 3c**), and as reported previously, samples
167 from patients admitted to the ICU had reduced diversity (-3.9, $p<0.05$, two-tailed T-test,
168 **Extended Data Fig. S5a**). However, the composition in samples between the two centers did not
169 show systematic compositional differences (**Fig. 3d,e,f**). On average, in both centers, members
170 of the phyla Firmicutes and Bacteroidetes represented the most abundant bacteria, followed by
171 Proteobacteria (**Fig. 3d**). The wide range of bacterial diversities was reflected in the high
172 variability of bacterial compositions across samples (**Fig. 3e,f**). In samples from both centers,
173 microbiome dominations, defined as a community where a single genus reached more than 50%
174 of the population, were observed frequently (NYU: 21 samples, YALE: 12 samples),
175 representing states of severe microbiome injury in COVID-19 patients (**Fig. 3g, Extended Data**

176 **Fig. S5a,b**). Strikingly, samples associated with a BSI, defined here as a positive clinical blood
177 culture test result, had strongly reduced bacterial α-diversities (mean difference: -5.2, CI_{BEST}[-
178 8.2, -2.2], **Fig. 3h**).
179 The lower diversity associated with samples from 25 patients (15 NYU, 10 Yale) with
180 BSIs led us to investigate their bacterial taxon compositions and the potential that gut dysbiosis
181 was associated with BSI events. Importantly, BSI patients had received antibiotic treatments
182 during hospitalization (**Extended Data Fig. S6, Supplementary Table 2**), which could
183 exacerbate COVID-19 induced shifts in microbiota populations[16,17,20], and may indeed be
184 administered in response to a suspected or confirmed BSI. We noted that most BSI patients
185 received antibiotics prior to their BSI, with 6 out of 25 patients receiving antibiotics only after
186 detection of BSI. Principal coordinate analysis of all stool samples indicated that the BSI-
187 associated samples spanned a broad range of compositions (**Fig. 3h**). To identify bacterial
188 abundance patterns that consistently distinguished BSI from non-BSI-associated samples, we
189 performed a Bayesian logistic regression. The model estimated the association of the 10 most
190 abundant bacterial genera with BSI cases, i.e. it identified enrichment or depletion of bacterial
191 genera in BSI associated samples (**Fig. 3i**). This analysis revealed that the genus
192 *Faecalibacterium* was negatively associated with BSI (OR: -0.5, CI:[-0.86, -0.15]), which was
193 also observed when we included microbiome domination as an additional factor in the model
194 (**Extended Data Fig. S7a**). However, our analysis also included stool samples that were taken
195 only after a positive blood culture was obtained, calling into question the plausibility of gut
196 translocation; a complementary analysis only using stool samples obtained prior or on the same
197 day of a positive blood culture also identified *Faecalibacterium* as most negatively associated
198 with BSI (**Extended Data Fig. S7b**). Furthermore, a higher-resolution analysis using amplicon
199 sequencing variant (ASV) relative abundances as predictors of BSI (**Extended Data Fig. S7c,d**),
200 identified an ASV of the *Faecalibacterium* genus as most negatively associated with BSI, in
201 agreement with our main analysis. *Faecalibacterium* is an immunosupportive, short-chain fatty
202 acid producing genus that is a prominent member of the human gut microbiome[44–46], and its
203 reduction is associated with disruption to intestinal barrier function[47,48], perhaps via ecological
204 network effects[48].
205 To evaluate the effect size of the association between *Faecalibacterium* and BSIs, we
206 performed a counterfactual posterior predictive check. Using the average genus composition

207 found across all samples, we first computed the distribution of predicted BSI risks (**Fig. 3j**), and
208 compared this risk distribution with a hypothetical bacterial composition which increased
209 *Faecalibacterium* by 10% points. The predicted risk distributions associated with these two
210 compositions differed strongly (mean difference 15%, CI: [1%, 32%], **Fig. 3j**). Domination
211 states of the microbiome increase the risk for BSIs in immunocompromised cancer patients[18];
212 such dominations imply high relative abundances of single taxa, and therefore a low diversity.
213 Consistent with this, *Faecalibacterium* abundance was positively correlated with diversity (R:
214 0.55, $p<10^{-10}$, **Extended Data Fig. S8**) in our data set and as reported previously[44].
215 We therefore next investigated a direct association between the bacteria populating the
216 gut microbiome and the organisms identified in the blood of patients. Visualizing the bacterial
217 composition in stool samples from patients alongside the BSI microorganisms (**Extended Data**
218 **Fig. S9a)** suggested a correspondence with the respective taxa identified in the blood: high
219 abundances of the BSI-causing microbes were found in corresponding stool samples. A rank
220 abundance analysis matching the organisms identified in clinical blood cultures to the
221 composition of bacteria in corresponding stool samples indicated enrichment of taxa belonging
222 to the same bacterial orders as BSI causing organisms (**Extended Data Fig. S9b**), suggesting
223 translocation of bacteria from the gut into the blood stream.
224 To further investigate evidence for translocation of gut bacteria into the blood, we next
225 performed shotgun metagenomic sequencing on a subset of BSI-associated samples with
226 sufficient remaining material in order to match the organism identified in clinical blood cultures
227 at the species level with reads obtained from stool samples (**Fig. 3k, Supplementary Table 3**).
228 In four cases of positive blood cultures of *Staphylococcus* species, no reads matching the
229 clinically identified species were detected (**Supplementary Table 3**). This may explain why the
230 rank analysis suggested that Staphylococcales were not generally enriched in BSIs by
231 *Staphylococcus* (**Extended Data Fig. S9a,b**). In all investigated cases of positive blood cultures
232 by other organisms, the species identified in clinical blood cultures had corresponding reads in
233 the stool samples. Furthermore, the relative abundances of matched species tended to be larger
234 than the average abundances of matched species across all samples (**Supplementary Table 3**).
235 Consistent with this, in one case of a *S. aureus* BSI where corresponding stool relative
236 abundances of *Staphylococcus* were low, reads from shotgun sequencing did not match the
237 genomes of isolates obtained from the same patient better than *S. aureus* genomes from other

238 isolates (**Extended Data Fig. S9d**). Strikingly, shotgun metagenomic reads matched the genome
239 of isolates well in another case where relative abundances of *Staphylococcus* were enriched in
240 the stool (**Extended Data Fig. S9c**), providing evidence that here, the same strains were found in
241 stool and blood of the same patient.

242 Collectively, these results reveal an unappreciated link between SARS-CoV-2 infection,
243 gut microbiome dysbiosis, and a severe complication of COVID-19, BSIs. The loss of diversity
244 and immunosupportive *Faecalibacterium* in patients with BSIs mirrored a similar loss of
245 diversity in the most severely sick mice deliberately infected with SARS-CoV-2, and as observed
246 by other labs and other model systems[49–51]. Notably, a recent study reproduced these changes in
247 the microbiome in an antibiotics-naïve cohort[52], suggesting that the viral infection causes gut
248 dysbiosis, either through gastrointestinal infection[53–57] or through a systemic inflammatory
249 response[2,4]. Furthermore, the pronounced increase in Akkermansiaceae in mice was also
250 observed in our patient samples, and has been reported previously in patients and in K18-hACE2
251 mice[49,58]. However, the dysbiosis in patients with COVID-19 exceeded the microbiota shifts
252 observed in the mouse experiments, including microbiome dominations by single taxa, which
253 was not seen in the mouse experiments. It is possible that in our experiment, mice were
254 sacrificed before perturbations to the gut microbial populations reached a maximum. hACE2
255 knock-in mice, which display reduced disease[37], were not tested in the scope of this study but
256 could provide additional insights in the future. However, it is also plausible that the frequently
257 administered antibiotic treatments that hospitalized COVID-19 patients receive exacerbated
258 SARS-CoV-2 induced microbiome perturbations. Additionally, unlike the controlled
259 environment experienced by laboratory mice, hospitalized patients are uniquely exposed to
260 antimicrobial-resistant infectious agents present on surfaces and shed by other patients.

261 Despite these limitations of the mouse model, we observed that SARS-CoV-2 infection
262 led to alteration of intestinal epithelial cells with established roles in intestinal homeostasis and
263 gastrointestinal disease[59,60]. Microbiome ecosystem shifts are likely both cause and consequence
264 of these epithelial cell alterations, since epithelial secretions are predicted to affect overall
265 community structure disproportionately strongly[61,62]. For example, disruption of Paneth cell-
266 derived antimicrobials including lysozyme are sufficient to impact microbiome composition[63–65],
267 and, conversely, *Akkermansia*, which was increased in infected mice, can have epithelium
268 remodeling properties[66].

269 Our observation that the type of bacteria that entered the bloodstream was enriched in the
270 associated stool samples is a well characterized phenomenon in cancer patients[18], especially
271 during chemotherapy induced leukocytopenia when patients are severely
272 immunocompromised[16,44]. COVID-19 patients are also immunocompromised and frequently
273 incur lymphopenia, rendering them susceptible to secondary infections[67]. Our data suggests
274 dynamics in COVID-19 patients may be similar to those observed in cancer patients: BSI-
275 causing organisms may translocate from the gut into the blood, potentially due to loss of gut
276 barrier integrity, through tissue damage downstream of antiviral immunity rather than
277 chemotherapy. Consistent with this possibility, soluble immune mediators such as TNFα and
278 interferons produced during viral infections, including SARS-CoV-2, damage the intestinal
279 epithelium to disrupt the gut barrier, especially when the inflammatory response is sustained as
280 observed in patient with severe COVID-19[43,68,69]. Indeed, blood plasma in severely sick COVID-
281 19 patients are enriched for markers of disrupted barrier integrity and higher levels of
282 inflammation markers[70], suggesting microbial translocation. Our data supports this model with
283 direct evidence because we were able to match sequencing reads from stool samples to genomes
284 of species detected in the blood of patients.
285 One limitation of our data is temporal ordering of samples. Occasionally stool samples
286 were collected after observation of BSI, and this mismatch in temporal ordering is counter
287 intuitive for gut-to-blood translocation and a causal interpretation of our associations. However,
288 the reverse direction, that blood infection populates and changes the gut community, is unlikely
289 for the organisms identified in the blood, and if our associations were not causal, we would
290 expect no match between BSI organisms and stool compositions.
291 Taken together, our findings support a scenario in which gut-to-blood translocation of
292 microorganisms following microbiome dysbiosis, a known issue for chronic conditions such as
293 cancer, leads to dangerous BSIs during COVID-19. We suggest that investigating the underlying
294 mechanism behind our observations will inform the judicious application of antibiotics and
295 immunosuppressives in patients with respiratory viral infections and increase our resilience to
296 pandemics.
297
298 **Materials and Methods**
299 *Bioethics statement*

300 The collection of COVID-19 human biospecimens for research has been approved by the
301 NYUSOM Institutional Review Board under il8-01121 Inflammatory Bowel Disease and Enteric
302 Infection at NYU Langone Health. The data presented in this study were also approved by Yale
303 Human Research Protection Program Institutional Review Boards (FWA00002571, protocol ID
304 2000027690). Informed consent was obtained from all enrolled patients.
305
306 *Mouse experiments*
307 Cells & virus
308 Vero E6 (CRL-1586; American Type Culture Collection) were cultured Dulbecco's Modified
309 Eagle's Medium (DMEM, Corning) supplemented with 10% fetal bovine serum (FBS, Atlanta
310 Biologics) and 1% nonessential amino acids (NEAA, Corning). SARS-CoV-2, isolate USA-
311 WA1/2020 19 (BEI resources #NR52281), a gift from Dr. Mark Mulligan at the NYU Langone
312 Vaccine Center was amplified once in Vero E6cells. All experiments with SARS-CoV-2 were
313 conducted in the NYU Grossman School of Medicine ABSL3 facility in accordance with its
314 Biosafety Manual and Standard Operating Procedures, by personnel equipped with powered air-
315 purifying respirators.
316
317 Mice
318 Heterozygous K18-hACE2 C57BL/6J mice (strain: 2B6.Cg-Tg(K18-ACE2)2Prlmn/J) were
319 obtained from The Jackson Laboratory. Several were paired with C57BL/6J mice to generate
320 additional heterozygous mice for subsequent experiments and the remaining were used to
321 perform initial experiments. Animals from the same breeder pool (i.e., littermates) were
322 randomly assigned and housed in cages according to the experimental groups and fed standard
323 chow diets. Cage bedding was mixed prior to infection in a subset of experiments to further
324 reduce possible cage effect. All animal studies were performed according to protocols approved
325 by the NYU School of Medicine Institutional Animal Care and Use Committee (IACUC
326 n°170209 and 180802) and in the ABSL3 facility of NYU Grossman School of Medicine (New
327 York, NY), in accordance with its Biosafety Manual and Standard Operating Procedures. 12-
328 week-old or 24-week-old K18-hACE2 males were administered either 10-10000 PFU SARS-
329 CoV-2 diluted in 50µL PBS (Corning) or 50µL PBS (non-infected, 0) via intranasal
330 administration under xylazine-ketamine anesthesia (AnaSedR AKORN Animal Health,

331 KetathesiaTM Henry Schein Inc). Viral titer in the inoculum was verified by plaque assay in
332 Vero E6 cells. Following infection, mice were monitored daily for weight loss, temperature loss
333 and signs of disease. A disease score was calculated as the sum of scores obtained for each of the
334 following criteria: ruffled fur (no= 0, yes=1), hunched back (no=0, slightly=1, exacerbated=2),
335 heavy breathing (no=0, yes=1), altered mobility (no=1, reduced activity=1, no mobility=2). Stool
336 samples were collected and stored at -80°C.
337
338 Measurement of viral load
339 Whole lungs and 1cm of proximal duodenum, terminal ileum and proximal colon were collected
340 five-to seven days after infection. Intestinal pieces were wash with PBS and all organs were
341 transferred in Eppendorf tubes containing 500µl of PBS and a 5mm stainless steel bead (Qiagen)
342 and h C57BL/6J mice omogenized using the Qiagen TissueLyser II. Homogenates were cleared
343 for 5 min at 5,000 × g, and the viral supernatant or nasal wash was diluted 4X in TRIzol reagent
344 (Invitrogen) and frozen at -80°C for titration by qRT-PCR. RNA was extracted from the TRIzol
345 homogenates using chloroform separation and isopropanol precipitation, followed by additional
346 purification using RNeasy spin columns with DNase treatment according to the manufacturer's
347 instructions (Rneasy Mini Kit; RNAse-Free DNase Set; QIAGEN). RNA was reverse-
348 transcribed using the High-Capacity cDNA Reverse Transcription Kit (Applied Biosystems).
349 qPCR was performed using Applied Biosystems TaqMan RNA-to-CT One-Step Kit (Fisher-
350 Scientific), 500nM of the primers (Fwd 5'-ATGCTGCAATCGTGCTACAA-3', Rev 5'-
351 GACTGCCGCCTCTGCTC-3') and 100nM of the N probe (5'-/56-
352 FAM/TCAAGGAAC/ZEN/AACATTGCCAA/3IABkFQ/-3'). Serial dilutions of *in-vitro* transcribed
353 RNA of the SARS-CoV-2 Nucleoprotein (generated as previously described[71]) were used to
354 generate a standard curve and calculate copy numbers per ug of RNA in the samples.
355
356 Microscopy
357 5cm of proximal duodenum, distal ileum and entire colon were flushed with 10% acetate
358 buffered formalin (Fisher scientific), cut open along the length, pinned on black wax and fixed
359 with formalin for 72hrs at RT. 2 cm strips of intestinal tissues were embedded in low melting
360 point agarose (Promega) to enrich for well-oriented crypt-villus units. Paraffin embedding,
361 sectioning, and staining were performed by the NYU Experimental Pathology Research

362 Laboratory. 5um sections were stained with hematoxylin and eosin (H&E) and imaged using
363 brightfield wholeslide scanning. Lysozyme staining was performed using anti-lysozyme
364 (ab108508, Abcam) and DAPI immunostaining and analyzed using a Zeiss AxioObserver.Z1
365 with Axiocam 503 Mono operated with Zen Blue software. 50 small intestinal villi per mouse
366 were measured for villi length. Goblets cell were quantified from 50 villus-crypt units (one villus
367 + half of the 2 surrounding crypts) per mouse. Paneth cells numbers and lysozyme staining
368 patterns were quantified from 50 crypts per mouse. Previously defined criteria were used to
369 quantify the proportion of Paneth cells displaying abnormal lysozyme staining[43]. Mean values
370 were calculated for each mouse and used as individual data points.
371
372 Measurement of intestinal permeability
373 Mice were fasted for 4hrs before oral gavage with 200uL of fluorescein isothiocyanate (FITC)-
374 dextran (3-5 kDa, Sigma-Aldrich) dissolved in sterile PBS (60mg/ml). After 4 hrs, mice were
375 euthanized and blood was collected by cardiac puncture. FITC-dextran in plasma was quantified
376 using a plate reader (excitation, 485 nm; emission, 530 nm). Citrulline, intestinal fatty acid-
377 binding protein, and lipopolysaccharide (LPS)-binding protein were quantified in the plasma by
378 enzyme-linked immunosorbent assay (ELISA) according to the manufacturer's instructions
379 (MyBioSource, CA).
380
381 Time series analyses of bacterial family abundances
382 We $\log_{10}$-transformed bacterial relative abundances adding a pseudo count to fill zeros ($2*10^{-6}$,
383 as done before). We then analyzed the time series with the following model that included fixed
384 effects for the intercepts and slopes of the treatment (i.e. indicator variables for uninfected (0
385 PFU), and infected (10000PFU), and random effects per cage and per mice to account for cage
386 effects and repeated measurements from the same individual mouse, respectively. The model
387 was implemented in the R programming language using the lmer function of the lme4 library
388 with the following model formula:
389 $$\log X_i \sim 1 + \text{PFU} + \text{time:PFU} + (1|\text{cage}) + (\text{time}|\text{mouseid})$$
390
391 *Human study*
392 Study population and data collection

393 This study involved 96 patients with laboratory-confirmed SARS-CoV-2 infection. SARS-CoV-
394 2 infection was confirmed by a positive result of real-time reverse transcriptase-polymerase
395 chain reaction assay on a nasopharyngeal swab. 60 patients were seen at NYU Langone Health,
396 New York, between January 29, 2020 – July 2, 2020. In order to be eligible for inclusion in the
397 study, stool specimens needed to be from individuals >18 years of age. Data including
398 demographic information, clinical outcomes, and laboratory results were extracted from the
399 electronic medical records in the NYU Langone Health clinical management system. Blood and
400 stool samples were collected by hospital staff. OmnigeneGut kits were used on collected stool. In
401 parallel, 36 patients were admitted to YNHH with COVID-19 between 18 March 2020 and 27
402 May 2020 as part of the YALE IMPACT cohort described at length elsewhere[2]. Briefly,
403 participants were enrolled after providing informed consent and paired blood and stool samples
404 were collected longitudinally where feasible for duration of hospital admission. No statistical
405 methods were used to predetermine sample size for this cohort. Demographic information of
406 patients was aggregated through a systematic and retrospective review of the EHR and was used
407 to construct **Supplementary Table 1**. Symptom onset and etiology were recorded through
408 standardized interviews with patients or patient surrogates upon enrolment in our study, or
409 alternatively through manual EHR review if no interview was possible owing to clinical status at
410 enrolment. The clinical data were collected using EPIC EHR and REDCap 9.3.6 software. At the
411 time of sample acquisition and processing, investigators were blinded to patient clinical status.
412
413 <u>DNA extraction and bacterial 16S rRNA sequencing</u>
414 For bacterial DNA extraction 700µL of SL1 lysis buffer (NucleoSpin Soil kit, Macherey-Nagel)
415 was added to the stool samples and tubes were heated at 95°C for 2h to inactivate SARS-CoV-2.
416 Samples were then homogenized using the FastPrep-24TM instrument (MP Biomedicals) and
417 extraction was pursued using the NucleoSpin Soil kit according to the manufacturer's
418 instructions. DNA concentration was assessed using a NanoDrop spectrophotometer. Samples
419 with too low DNA concentration were excluded. DNA from human samples was extracted with
420 PowerSoil Pro (Qiagen) on the QiaCube HT (Qiagen), using Powerbead Pro (Qiagen) plates with
421 0.5mm and 0.1mm ceramic beads. For mouse samples, the variable region 4 (V4) of the 16S
422 rRNA gene was amplified by PCR using primers containing adapters for MiSeq sequencing and
423 single-index barcodes. All PCR products were analyzed with the Agilent TapeStation for quality

424 control and then pooled equimolar and sequenced directly in the Illumina MiSeq platform using
425 the 2x250 bp protocol. Human samples were prepared with a protocol derived from [72], using
426 KAPA HiFi Polymerase to amplify the V4 region of the 16S rRNA gene. Libraries were
427 sequenced on an Illumina MiSeq using paired-end 2x250 reads and the MiSeq Reagent Kitv2.
428
429 Bioinformatic processing and taxonomic assignment
430 Amplicon sequence variants (ASVs) were generated via dada2 v1.16.0 using post-QC FASTQ
431 files. Within the workflow, the paired FASTQ reads were trimmed, and then filtered to remove
432 reads containing Ns, or with maximum expected errors >= 2. The dada2 learn error rate model
433 was used to estimate the error profile prior to using the core dada2 algorithm for inferring the
434 sample composition. Forward and reverse reads were merged by overlapping sequence, and
435 chimeras were removed before taxonomic assignment. ASV taxonomy was assigned up to genus
436 level using the SILVAv.138 database with the method described in [73] and a minimum
437 boostrapping support of 50%. Species-level taxonomy was assigned to ASVs only with 100%
438 identity and unambiguous matching to the reference.
439
440 Shotgun metagenomic sequencing
441 DNA was quantified with Qiant-iT Picogreen dsDNA Assay (Invitrogen). Libraries were
442 prepared with a procedure adapted from the Nextera Library Prep kit (Illumina), and sequenced
443 on an Illumina NovaSeq using paired-end 2x150 reads (Illumina) aiming for 100M read depth.
444 DNA sequences were filtered for low quality (Q-Score < 30) and length (< 50), and adapter
445 sequences were trimmed using cutadapt. Fastq files were converted a single fasta using shi7.
446 Sequences were trimmed to a maximum length of 100 bp prior to alignment. DNA sequences
447 were taxonomically classified using the MetaPhlAn2 analysis tool
448 (http://huttenhower.sph.harvard.edu/metaphlan2). MetaPhlAn2 maps reads to clade-specific
449 marker genes identified from ~17,000 reference genomes and estimates clade abundance within a
450 sample from these mappings.
451
452 Mapping shotgun reads to whole genome sequences of clinical isolates
453 Quality-controlled reads were re-classified using Kraken2 (Minikraken2 v2 database, available
454 on https://ccb.jhu.edu/software/kraken2/index.shtml). Reads that were classified by Kraken2 as

455 *Staphylococcus aureus* (or a strain thereof) were further mapped using Bowtie2 separately to
456 each of a collection of *Staphylococcus aureus* isolates. The collection was composed of all NCBI
457 RefSeq assemblies as of 11/17/2021, in addition to *Staphylococcus aureus* isolates that were
458 isolated from our subjects. Bowtie2 mapped reads were then further filtered, keeping only reads
459 that mapped without mismatches. A neighbor-joining (NJ) tree was produced from this
460 collection of genomes using Snippy (https://github.com/tseemann/snippy).
461
462 *Compositional analyses*
463 <u>α-Diversity</u>
464 We calculated the inverse Simpson (*IVS*) index from relative ASV abundances (*p*) with *N* ASVs
465 in a given sample, $IVS = \frac{1}{\sum_i^N p_i^2}$.
466 <u>Principal Coordinate Analyses</u>
467 Bray-Curtis distances were calculated from the filtered ASV table using QIIME 1.9.1 and
468 principal components of the resulting distance matrix were calculated using the scikit-learn
469 package for the Python programming language, used to embed sample compositions in the first
470 two principal coordinates.
471
472 <u>Average compositions and manipulation of compositions</u>
473 To describe the average composition of a set of samples we calculated the central tendency of a
474 compositional sample [74]. For counter factual statistical analyses that require changes to a
475 composition, e.g. an increase in a specific taxon, we deployed the perturbation operation (⊕),
476 which is the compositional analogue to addition in Euclidean space[74]. A sample *x* containing the
477 original relative taxon abundances is perturbed by a vector *y*,
478 $$y\colon\ x \oplus y = \left[\frac{x_1 y_1}{\sum_{i=1}^{D} x_i y_i}, \frac{x_2 y_2}{\sum_{i=1}^{D} x_i y_i}, \ldots, \frac{x_D y_D}{\sum_{i=1}^{D} x_i y_i}\right] \forall x, y \in S^D$$
479 where S^D represents the D-part simplex.
480
481 <u>Bayesian t-test</u>
482 To compare diversity measurements between different sample groups, e.g. different clinical
483 status, we performed a Bayesian estimation of group differences (BEST, [75]) , implemented using

484 the pymc3 package for the Python programming language; with priors (∼) and deterministic
485 calculations (=) to assess differences in estimated group means as follows:

486 $g_1 \sim \text{Normal}(\mu = 15, \sigma = 15)$
487 $g_2 \sim \text{Normal}(\mu = 15, \sigma = 15)$
488 $\sigma_{g1} \sim \text{Uniform}(\text{low} = 1e{-}4, \text{high} = 30)$
489 $\sigma_{g2} \sim \text{Uniform}(\text{low} = 1e{-}4, \text{high} = 30)$
490 $\nu \sim \text{Exponential}(1/15) + 1$
491 $\lambda_1 = \sigma_{g1}^{-2}$
492 $\lambda_2 = \sigma_{g2}^{-2}$
493 $G1 \sim \text{StudentT}(\text{nu} = \nu, \text{mu} = g_1, \text{lam} = \lambda_1)$
494 $G2 \sim \text{StudentT}(\text{nu} = \nu, \text{mu} = g_2, \text{lam} = \lambda_2)$
495 $\Delta = G1 - G2$

496 Bayesian inference was performed using "No U-turn sampling"[76]. Highest density intervals
497 (HDI) of the posterior estimation of group differences (Δ) were used to determine statistical
498 certainty (***: 99% HDI >0 or <0, **: 95%HDI, *:90% HDI). The BEST code was implemented
499 following the pymc3 documentation.
500

501 <u>Cross-validated logistic regression to associate BSI cases with ASV composition</u>
502 We first removed ASVs with low prevalence (present in fewer than 5% of all samples), and low
503 abundances (maximum observed relative abundance <0.01) leaving 269 ASVs. We then scaled
504 the ASV relative abundances between 0 and 1 (min-max scaling) and performed logistic
505 regressions, relating ASV abundances to BSI status (1: BSI, 0: non-BSI) using the
506 sklearn.linear_model. LogisticRegressionCV module for the Python programming language with
507 an L1 (lasso) penalty, iterating over a range of regularization strengths ([0.01,0.1, 1., 10., 100.,
508 1000.]) using the "liblinear" solver. We retained the inferred ASV association coefficients with
509 non-zero values for each tested regularization strength to visualize the cross-validation path.
510

511 <u>Bayesian logistic regression</u>
512 We performed a Bayesian logistic regression to distinguish compositional differences between
513 infection-associated samples and samples from patients without secondary infections. We
514 modeled the infection state of patient sample *i*, *yi* with a Binomial likelihood:

$$y_i \sim \text{Binomial}(n = 1, p = p)$$

$$p = \text{inverse logistic}(\alpha + X_i\beta)$$

$$\alpha \sim \text{Normal}(\mu = 0, \sigma = 1)$$

$$\beta \sim \text{Normal}(\mu = 0, \sigma = 1)$$

Where prior distributions are indicated by ∼; α is the intercept of the generalized linear model, β is the coefficient vector for the $\log_{10}$-relative taxon abundances X_i in sample i or, in some cases, the binary indicator variable for gut microbiome domination.

524 **Data Availability**

525 The raw sequencing data have been deposited on the Sequencing Reads Archive (SRA), and SRA
526 accession numbers are available for two bioprojects corresponding to the mouse sequencing data
527 PRJNA745367 (**Supplementary Table 4**) and the human stool samples PRJNA746322
528 (**Supplementary Table 5**).

Figures

530

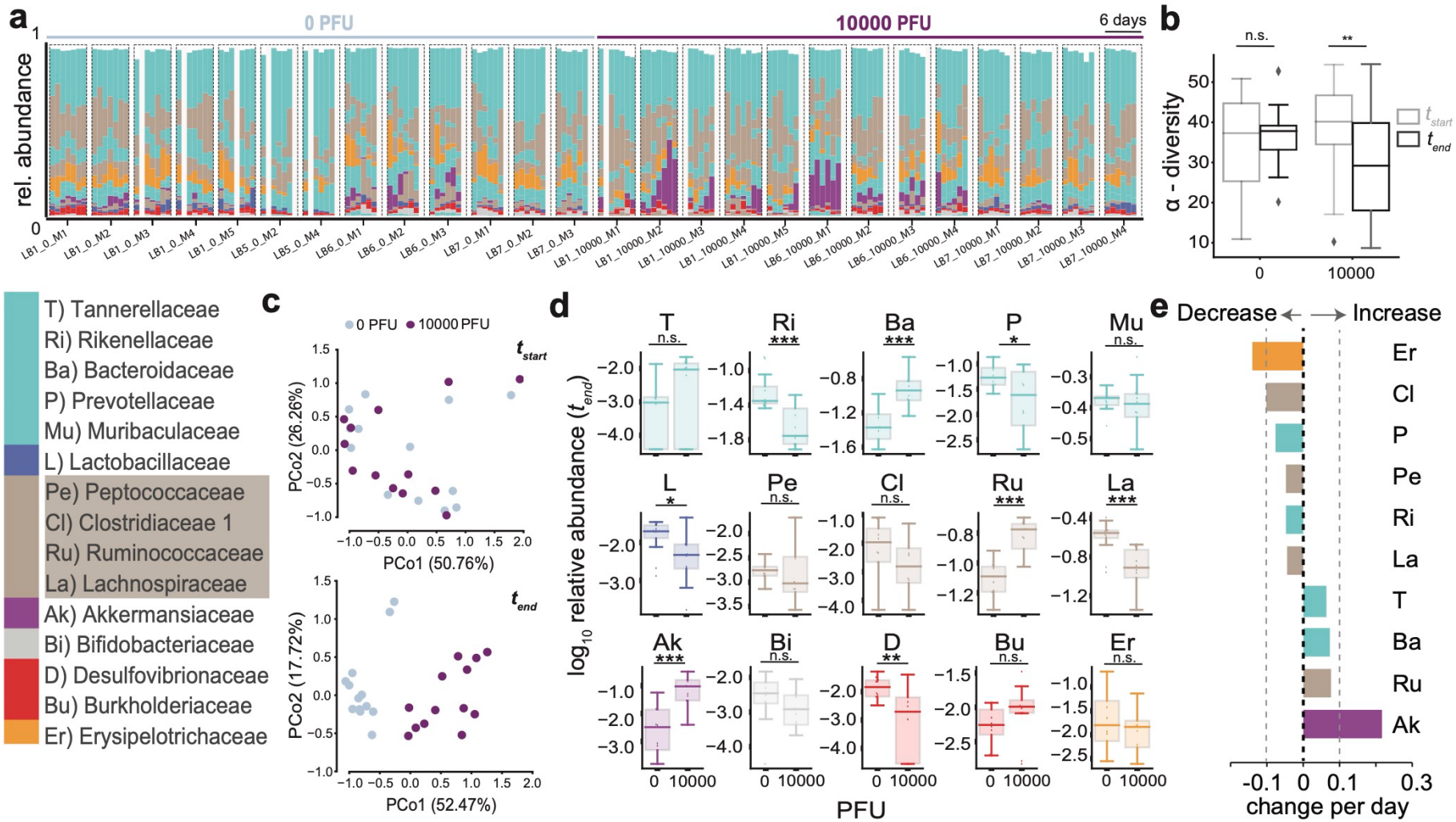
a
0 PFU
10000 PFU
6 days
rel. abundance
b
α - diversity
n.s.
**
t_{start}
t_{end}
T) Tannerellaceae
Ri) Rikenellaceae
Ba) Bacteroidaceae
P) Prevotellaceae
Mu) Muribaculaceae
L) Lactobacillaceae
Pe) Peptococcaceae
Cl) Clostridiaceae 1
Ru) Ruminococcaceae
La) Lachnospiraceae
Ak) Akkermansiaceae
Bi) Bifidobacteriaceae
D) Desulfovibrionaceae
Bu) Burkholderiaceae
Er) Erysipelotrichaceae
c
0 PFU
10000 PFU
PCo2 (26.26%)
PCo1 (50.76%)
PCo2 (17.72%)
PCo1 (52.47%)
d
$\log_{10}$ relative abundance (t_{end})
PFU
e
Decrease
Increase
change per day

531

532 **Fig. 1. SARS-CoV-2 infection causes gut microbiome alterations in mice**. **a** Timelines of
533 fecal microbiota composition measured by 16S rRNA gene sequencing in mice infected with 0 or
534 10^4 PFU of SARS-CoV-2 ; time of infection=Day 1. Bars represent the composition of the 15
535 most abundant bacterial families per sample, blocks of samples correspond to an individual
536 mouse's time course (x-axis label indicate experiment id, PFU, and mouse id). **b** α-diversity
537 (inverse Simpson index) per infection group in the beginning (t_{start}) and at the end (t_{end}) of the
538 experiment (n.s.: non-significant, **: p<0.01, one-tailed, paired t-test). **c** Principal coordinate
539 plot of bacterial compositions in samples from the start (top) and end (bottom) of the experiment.
540 **d** log_{10}-relative family abundances at the final time point; boxplots show median and
541 interquartile ranges, whiskers extend to 1.5 times max- and min- quartile values, n.s.: not
542 significant; *: p-value < 0.05; **: p-value < 0.01; ***: p-value < 0.001; Wilcoxon rank-sum
543 tests. **e** Regression coefficients of the estimated changes in family abundances per day in mice
544 infected with 10^4 PFU obtained from linear mixed effects models with varying effects per mouse
545 and per cage (only significant coefficient results shown, abbreviations and colors as per the
546 bacterial family legend).
547
548

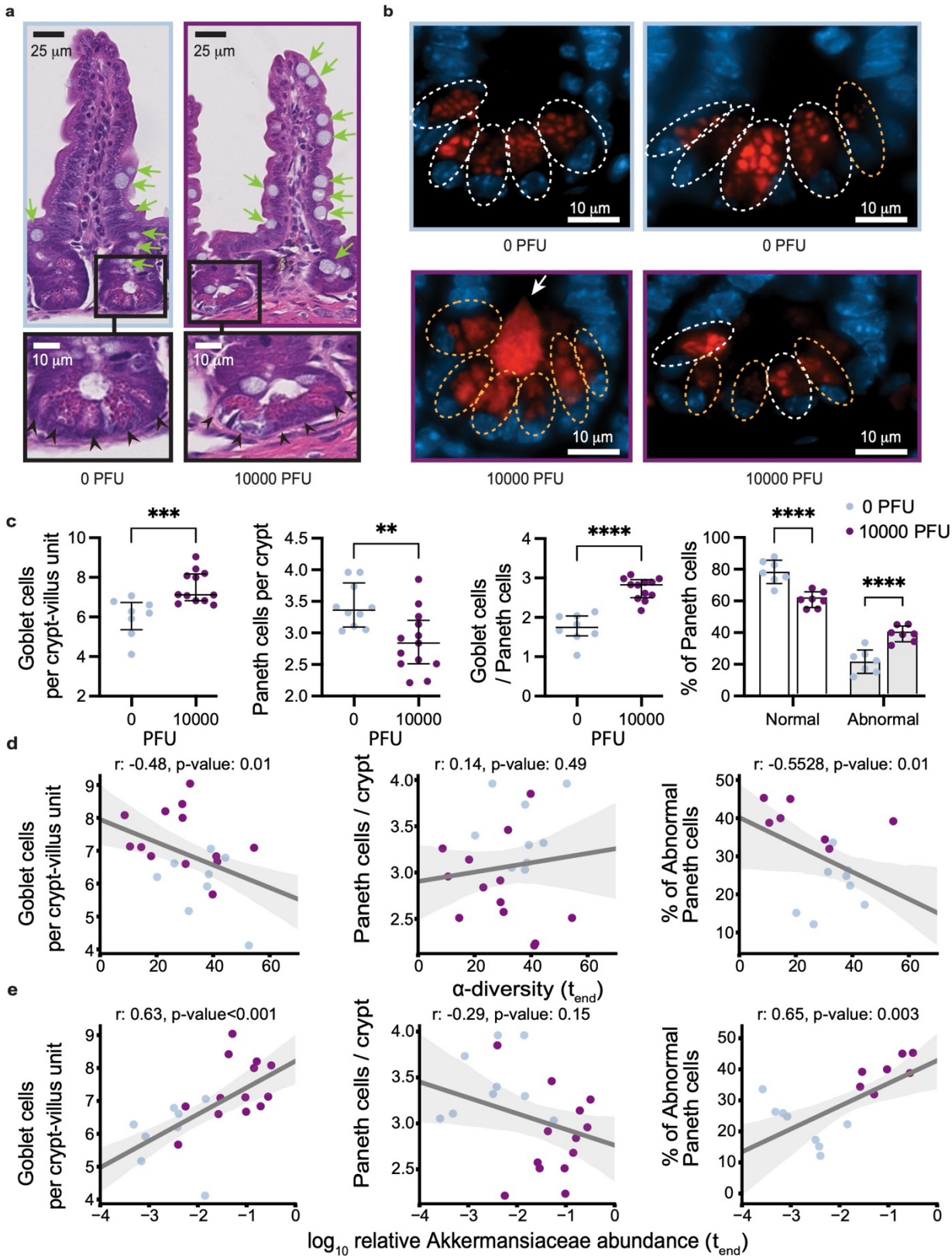
a
25 µm
25 µm
10 µm
10 µm
0 PFU
10000 PFU
b
10 µm
0 PFU
0 PFU
10 µm
10 µm
10000 PFU
10000 PFU
c
Goblet cells per crypt-villus unit
***
PFU
Paneth cells per crypt
**
Goblet cells / Paneth cells
****
% of Paneth cells
****
****
0 PFU
10000 PFU
Normal
Abnormal
d
r: -0.48, p-value: 0.01
Goblet cells per crypt-villus unit
r: 0.14, p-value: 0.49
Paneth cells / crypt
r: -0.5528, p-value: 0.01
% of Abnormal Paneth cells
α-diversity (t_{end})
e
r: 0.63, p-value<0.001
Goblet cells per crypt-villus unit
r: -0.29, p-value: 0.15
Paneth cells / crypt
r: 0.65, p-value: 0.003
% of Abnormal Paneth cells
$\log_{10}$ relative Akkermansiaceae abundance (t_{end})

549

550 **Fig. 2 SARS-CoV-2 infection causes abnormalities in the gut epithelium of mice. a.**
551 Representative H&E-stained section of the ileum depicting crypt-villus axes from K18-hACE2
552 mice on day 5-6 post intranasal inoculation with 10000 PFU SARS-CoV-2 or mock treatment.
553 Green arrows indicate goblet cells, scale bars correspond to 25μm. Bottom panels show high
554 magnification images of the indicated crypt with black arrowheads pointing at Paneth cells, scale
555 bars correspond to 10μm. **b.** Representative anti-lysozyme immunofluorescence images of the
556 ileal crypt (two images per group). White and orange doted circles delineate normal and
557 abnormal Paneth cells, respectively. Abnormality is characterized by distorted, depleted, or
558 diffuse lysozyme distribution patterns in Paneth cells. Lysozyme = red, DAPI = blue, scale bars
559 correspond to 10□m. **c.** Quantification of goblet cell number per villus (left), Paneth cells per
560 crypt (middle) based on H&E staining, and frequency of normal versus abnormal Paneth cell
561 lysozyme distribution pattern based on the immunofluorescence staining as depicted in b. Dots
562 represent the mean cell number per crypt-villus unit in each mouse, 50 units were counted per
563 mouse. Results were pooled from 3 independent experiments with n=3-5 mice per group for each
564 experiment. Boxplots indicate median and interquartile ranges (ns=non-significant, $p>0.05$; **,
565 $p<0.01$; ***, $p<0.001$; ****, $p<0.0001$ Mann-Whitney U-test). **d.** Correlation of Goblet cell
566 number per villus (left, Pearson correlation $r=-0.48$, $p=0.015$), Paneth cells per crypt (middle,
567 $r=0.14$, p-value=0.483) and frequency of abnormal Paneth cell lysozyme distribution pattern
568 (right, $r=-0.5528$, $p=0.014$) for the mice shown in c with α-diversity (inverse Simpson) of the gut
569 microbiome measured at the last day before sacrifice. **e.** Correlation of Goblet cell number per
570 villus (left, $r=0.63$, $p<0.001$), Paneth cells per crypt (middle, $r=-0.29$, $p=0.149$) and frequency of
571 abnormal Paneth cell lysozyme distribution pattern (right, $r=0.65$, p-value=0.003) for the mice
572 shown in c with $\log_{10}$-relative abundances of *Akkermansia* in fecal samples from the last day
573 before sacrifice; lines: univariate linear regression, shaded region: 95% CI.
574

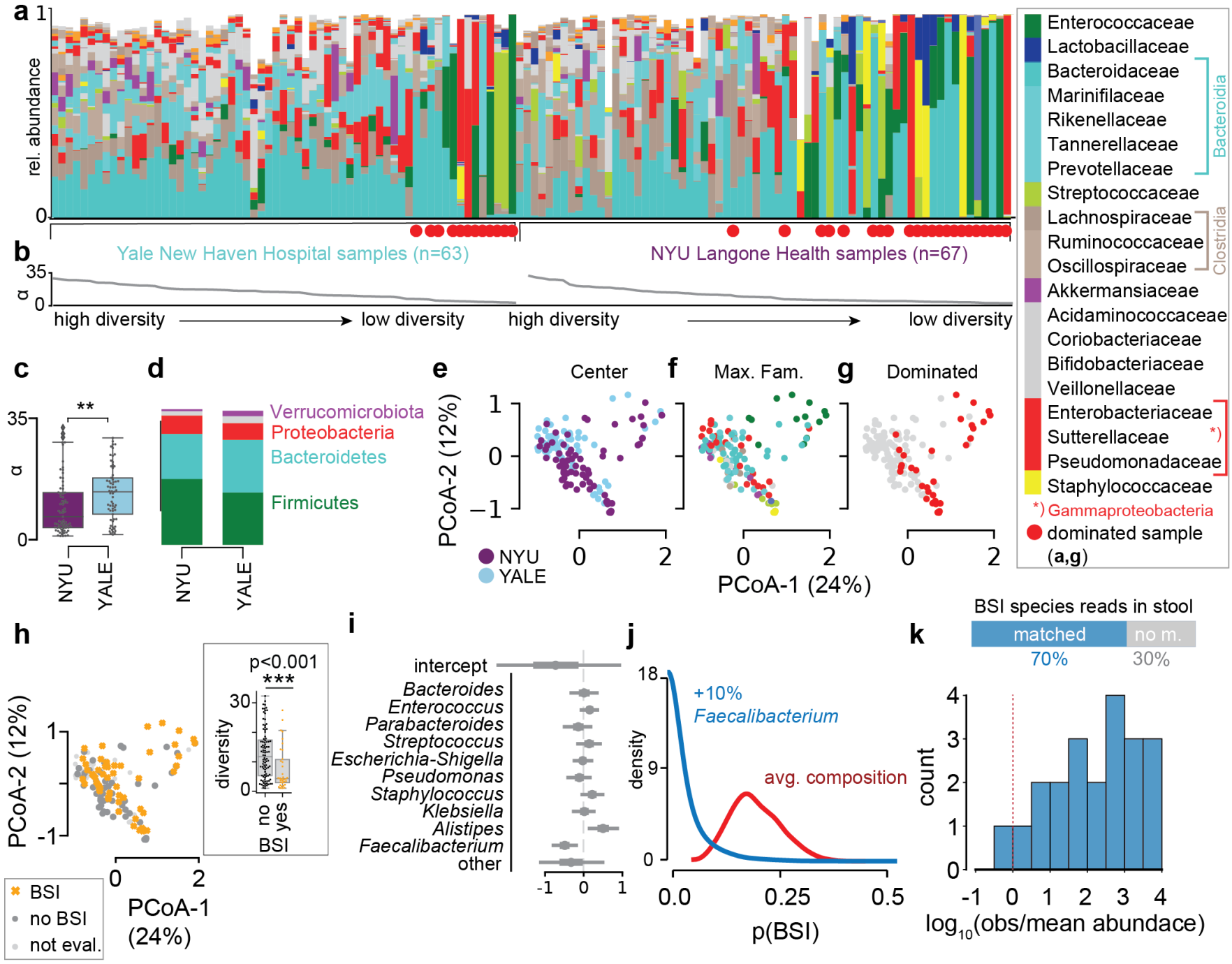
a
rel. abundance
1
0
Yale New Haven Hospital samples (n=63)
NYU Langone Health samples (n=67)
b
α
35
0
high diversity
low diversity
high diversity
low diversity
Enterococcaceae
Lactobacillaceae
Bacteroidaceae
Marinifilaceae
Rikenellaceae
Tannerellaceae
Prevotellaceae
Bacteroidia
Streptococcaceae
Lachnospiraceae
Ruminococcaceae
Oscillospiraceae
Clostridia
Akkermansiaceae
Acidaminococcaceae
Coriobacteriaceae
Bifidobacteriaceae
Veillonellaceae
Enterobacteriaceae
Sutterellaceae
Pseudomonadaceae
*)
Staphylococcaceae
*) Gammaproteobacteria
dominated sample (a,g)
c
α
35
0
**
NYU
YALE
d
Verrucomicrobiota
Proteobacteria
Bacteroidetes
Firmicutes
NYU
YALE
e
Center
f
Max. Fam.
g
Dominated
PCoA-2 (12%)
1
0
−1
NYU
YALE
0
2
PCoA-1 (24%)
h
PCoA-2 (12%)
1
-1
0
2
PCoA-1 (24%)
BSI
no BSI
not eval.
p<0.001
***
diversity
30
0
no
yes
BSI
i
intercept
Bacteroides
Enterococcus
Parabacteroides
Streptococcus
Escherichia-Shigella
Pseudomonas
Staphylococcus
Klebsiella
Alistipes
Faecalibacterium
other
-1
0
1
j
density
18
9
0
+10%
Faecalibacterium
avg. composition
0.0
0.25
0.5
p(BSI)
k
BSI species reads in stool
matched
no m.
70%
30%
count
4
3
2
1
0
-1
0
1
2
3
4
log10(obs/mean abundace)

575

576 **Fig. 3. The dysbiotic gut microbiome in COVID-19 in patients from NYU Langone Health**
577 **(n=60) and Yale New Haven Hospital (n=36) is associated with secondary bloodstream**
578 **infections**. **a** Bacterial family composition in stool samples (Yale, n = 63 samples; NYU, n = 67)
579 identified by 16S rRNA gene sequencing; bars represent the relative abundances of bacterial
580 families; red circles indicate samples with single taxa >50%. Samples are sorted by center and
581 bacterial α-diversity (inverse Simpson index, **b**). **c** α-diversity in samples from NYU Langone
582 Health and Yale New Haven Hospital; **p<0.01, two-sided T-test. **d** Average phylum level
583 composition per center. **e-g** Principal coordinate plots of all samples shown in **a**, labeled by center
584 (**e**), most abundant bacterial family (**f**) and domination status of the sample (**g**), and BSI status;
585 inset: boxplot of inverse Simpson index diversity by BSI (**h**). **i** Coefficients from a Bayesian
586 logistic regression with most abundant bacterial genera as predictors of BSI status. **j**
587 Counterfactual posterior predictions of BSI risk based on bacterial composition contrasting the
588 predicted risk of the average composition across all samples (red) with the risk predicted from a
589 composition where *Faecalibacterium* was increased by 10% (blue). **k** shotgun metagenomic reads
590 matched the species identified in clinical blood cultures in 70% of all investigated cases; the
591 histogram shows the distribution of $\log_{10}$-ratios of relative abundances of matched species in
592 corresponding stool samples to their corresponding mean abundances across all samples.

Acknowledgments

We thank René Niehus for helpful discussions on the implementation of the various Bayesian analyses. We thank the NYU Langone's Genome Technology Center, the NYU Langone's Experimental Pathology Research Laboratory and the NYU Langone's Microscopy Laboratory supported in part by NYU Langone Health's Laura and Isaac Perlmutter Cancer Center Support (grant P30CA016087) from the National Cancer Institute Langone and by the NIH S10 OD021747 grant for use of their instruments and technical assistance. We also thank the Office of Science & Research High-Containment Laboratories at NYU Grossman School of Medicine for their support in the completion of this research.

Yale IMPACT Team

Abeer Obaid, Alice Lu-Culligan, Allison Nelson, Anderson Brito, Angela Nunez, Anjelica Martin, Annie Watkins, Bertie Geng, Chaney Kalinich, Christina Harden, Codruta Todeasa, Cole Jensen, Daniel Kim, David McDonald, Denise Shepard, Edward Courchaine, Elizabeth B. White, Eric Song, Erin Silva, Eriko Kudo, Giuseppe DeIuliis, Harold Rahming, Hong-Jai Park, Irene Matos, Jessica Nouws, Jordan Valdez, Joseph Fauver, Joseph Lim, Kadi-Ann Rose, Kelly Anastasio, Kristina Brower, Laura Glick, Lokesh Sharma, Lorenzo Sewanan, Lynda Knaggs, Maksym Minasyan, Maria Batsu, Mary Petrone, Maxine Kuang, Maura Nakahata, Melissa Campbell, Melissa Linehan, Michael H. Askenase, Michael Simonov, Mikhail Smolgovsky, Nicole Sonnert, Nida Naushad, Pavithra Vijayakumar, Rick Martinello, Rupak Datta, Ryan Handoko, Santos Bermejo, Sarah Prophet, Sean Bickerton, Sofia Velazquez, Tara Alpert, Tyler Rice, William Khoury-Hanold, Xiaohua Peng, Yexin Yang, Yiyun Cao & Yvette Strong

Author contributions

LBR performed the mouse experiments with help from MGN, AMVJ. CZ performed mouse microbiome analyses with help from LBR, MV and KC. MV, JEA and JS prepared the samples from NYU. MV, JEA prepared the clinical data from NYU with help from JG, EW, BS. JK provided the data from Yale with help from ACM and the IMPACT team, AIK and AI. JS designed and performed the analyses with CZ, and help by GAH and APS. JS and KC designed the research question with support from VJT and BS. JS and KC wrote the manuscript with help

623 by LBR, MV and CZ. All other authors contributed materials, scientific feedback and
624 commented on the manuscript.
625
626 **Funding**
627 This work was in part funded by NYU Grossman School of Medicine startup research funds and
628 NIH/NIAID DP2 award (DP2AI164318) to JS, and the Yale School of Public Health and the
629 Beatrice Kleinberg Neuwirth Fund, as well as NIH grants to KC (DK093668, AI121244,
630 HL123340, AI130945, AI140754, DK124336), a Faculty Scholar grant from the Howard Hughes
631 Medical Institute (KC), Crohn's & Colitis Foundation (KC), Kenneth Rainin Foundation (KC),
632 Judith & Stewart Colton Center of Autoimmunity (KC). Further funding was provided by grants
633 from the NIH/NIAID to MD (R01AI143639 and R21AI139374), from the NIH to MV
634 (5T32AI100853), by Jan Vilcek/David Goldfarb Fellowship Endowment Funds to AMVJ, by
635 The G. Harold and Leila Y. Mathers Charitable Foundation to MD, and by NYU Grossman
636 School of Medicine Startup funds to MD and KAS, and the NYU Grossman School of Medicine
637 COVID-19 seed research funds to VJT, and funds from the NYU Langone Health Antimicrobial-
638 Resistant Pathogens Program to BS, AP, and VJT. KC and VJT also receive support from NIH
639 grant OT2HL161847. MN was supported by the American Heart Association Postdoctoral
640 Fellowship 19-A0-00-1003686. IMPACT received support from the Yale COVID-19 Research
641 Resource Fund. AI and DRL are Investigators of the Howard Hughes Medical Institute. AIK
642 received support from the Beatrice Kleinberg Neuwirth Fund, Bristol Meyers Squibb Foundation
643 and COVID-19 research funds from the Yale Schools of Public Health and Medicine.
644
645 **Conflicts**
646 KC has received research support from Pfizer, Takeda, Pacific Biosciences, Genentech, and
647 Abbvie; consulted for or received an honoraria from Puretech Health, Genentech, and Abbvie;
648 and holds U.S. patent 10,722,600 and provisional patents 62/935,035 and 63/157,225. JS is
649 cofounder of Postbiotics Plus Research LLC.
650

651 **Bibliography**

652

653 1. Fajgenbaum, D. C. & June, C. H. Cytokine Storm. *N. Engl. J. Med.* **383,** 2255–2273 (2020).
654 2. Lucas, C. *et al.* Longitudinal analyses reveal immunological misfiring in severe COVID-19.
655 *Nature* **584,** 463–469 (2020).
656 3. Zuo, T. *et al.* Alterations in Gut Microbiota of Patients With COVID-19 During Time of
657 Hospitalization. *Gastroenterology* **159,** 944–955.e8 (2020).
658 4. Yeoh, Y. K. *et al.* Gut microbiota composition reflects disease severity and dysfunctional
659 immune responses in patients with COVID-19. *Gut* **70,** 698–706 (2021).
660 5. Gu, S. *et al.* Alterations of the gut microbiota in patients with coronavirus disease 2019 or
661 H1N1 influenza. *Clin. Infect. Dis.* **71,** 2669–2678 (2020).
662 6. Nori, P. *et al.* Bacterial and fungal coinfections in COVID-19 patients hospitalized during
663 the New York City pandemic surge. *Infect. Control Hosp. Epidemiol.* **42,** 84–88 (2021).
664 7. Grasselli, G. *et al.* Hospital-Acquired Infections in Critically Ill Patients With COVID-19.
665 *Chest* (2021). doi:10.1016/j.chest.2021.04.002
666 8. Yu, D. *et al.* Low prevalence of bloodstream infection and high blood culture contamination
667 rates in patients with COVID-19. *PLoS One* **15,** e0242533 (2020).
668 9. Langford, B. J. *et al.* Bacterial co-infection and secondary infection in patients with
669 COVID-19: a living rapid review and meta-analysis. *Clin. Microbiol. Infect.* **26,** 1622–1629
670 (2020).
671 10. Shafran, N. *et al.* Secondary bacterial infection in COVID-19 patients is a stronger predictor
672 for death compared to influenza patients. *Sci. Rep.* **11,** 12703 (2021).
673 11. Buffie, C. G. *et al.* Precision microbiome reconstitution restores bile acid mediated
674 resistance to Clostridium difficile. *Nature* **517,** 205–208 (2015).
675 12. Buffie, C. G. & Pamer, E. G. Microbiota-mediated colonization resistance against intestinal
676 pathogens. *Nat. Rev. Immunol.* **13,** 790–801 (2013).
677 13. Modi, S. R., Collins, J. J. & Relman, D. A. Antibiotics and the gut microbiota. *J. Clin.*
678 *Invest.* **124,** 4212–4218 (2014).
679 14. Shimasaki, T. *et al.* Increased Relative Abundance of Klebsiella pneumoniae
680 Carbapenemase-producing Klebsiella pneumoniae Within the Gut Microbiota Is Associated
681 With Risk of Bloodstream Infection in Long-term Acute Care Hospital Patients. *Clin. Infect.*
682 *Dis.* **68,** 2053–2059 (2019).
683 15. Kim, S., Covington, A. & Pamer, E. G. The intestinal microbiota: Antibiotics, colonization
684 resistance, and enteric pathogens. *Immunol. Rev.* **279,** 90–105 (2017).
685 16. Morjaria, S. *et al.* Antibiotic-Induced Shifts in Fecal Microbiota Density and Composition
686 during Hematopoietic Stem Cell Transplantation. *Infect. Immun.* **87,** (2019).
687 17. Niehus, R. *et al.* Quantifying antibiotic impact on within-patient dynamics of extended-
688 spectrum beta-lactamase resistance. *Elife* **9,** (2020).
689 18. Taur, Y. *et al.* Intestinal domination and the risk of bacteremia in patients undergoing
690 allogeneic hematopoietic stem cell transplantation. *Clin. Infect. Dis.* **55,** 905–914 (2012).
691 19. Taur, Y. *et al.* Reconstitution of the gut microbiota of antibiotic-treated patients by
692 autologous fecal microbiota transplant. *Sci. Transl. Med.* **10,** (2018).
693 20. Liao, C. *et al.* Compilation of longitudinal microbiota data and hospitalome from
694 hematopoietic cell transplantation patients. *Sci. Data* **8,** 71 (2021).
695 21. Peled, J. U. *et al.* Microbiota as Predictor of Mortality in Allogeneic Hematopoietic-Cell
696 Transplantation. *N. Engl. J. Med.* **382,** 822–834 (2020).

697 22. McCullers, J. A. The co-pathogenesis of influenza viruses with bacteria in the lung. *Nat.*
698 *Rev. Microbiol.* **12,** 252–262 (2014).
699 23. Wang, D. *et al.* Clinical Characteristics of 138 Hospitalized Patients With 2019 Novel
700 Coronavirus-Infected Pneumonia in Wuhan, China. *JAMA* **323,** 1061–1069 (2020).
701 24. Westblade, L. F., Simon, M. S. & Satlin, M. J. Bacterial coinfections in coronavirus disease
702 2019. *Trends Microbiol.* **29,** 930–941 (2021).
703 25. Sepulveda, J. *et al.* Bacteremia and Blood Culture Utilization during COVID-19 Surge in
704 New York City. *J. Clin. Microbiol.* **58,** (2020).
705 26. Lansbury, L., Lim, B., Baskaran, V. & Lim, W. S. Co-infections in people with COVID-19:
706 a systematic review and meta-analysis. *J. Infect.* **81,** 266–275 (2020).
707 27. Sieswerda, E. *et al.* Recommendations for antibacterial therapy in adults with COVID-19 -
708 an evidence based guideline. *Clin. Microbiol. Infect.* **27,** 61–66 (2021).
709 28. Zhai, B. *et al.* High-resolution mycobiota analysis reveals dynamic intestinal translocation
710 preceding invasive candidiasis. *Nat. Med.* **26,** 59–64 (2020).
711 29. Haak, B. W. *et al.* Impact of gut colonization with butyrate-producing microbiota on
712 respiratory viral infection following allo-HCT. *Blood* **131,** 2978–2986 (2018).
713 30. Deriu, E. *et al.* Influenza Virus Affects Intestinal Microbiota and Secondary Salmonella
714 Infection in the Gut through Type I Interferons. *PLoS Pathog.* **12,** e1005572 (2016).
715 31. Yildiz, S., Mazel-Sanchez, B., Kandasamy, M., Manicassamy, B. & Schmolke, M. Influenza
716 A virus infection impacts systemic microbiota dynamics and causes quantitative enteric
717 dysbiosis. *Microbiome* **6,** 9 (2018).
718 32. Steed, A. L. *et al.* The microbial metabolite desaminotyrosine protects from influenza
719 through type I interferon. *Science* **357,** 498–502 (2017).
720 33. Abt, M. C. *et al.* Commensal bacteria calibrate the activation threshold of innate antiviral
721 immunity. *Immunity* **37,** 158–170 (2012).
722 34. Ichinohe, T. *et al.* Microbiota regulates immune defense against respiratory tract influenza A
723 virus infection. *Proc. Natl. Acad. Sci. USA* **108,** 5354–5359 (2011).
724 35. Sencio, V. *et al.* Influenza infection impairs the gut's barrier properties and favors secondary
725 enteric bacterial infection through reduced production of short-chain fatty acids. *Infect.*
726 *Immun.* (2021). doi:10.1128/IAI.00734-20
727 36. Wang, J. *et al.* Respiratory influenza virus infection induces intestinal immune injury via
728 microbiota-mediated Th17 cell-dependent inflammation. *J. Exp. Med.* **211,** 2397–2410
729 (2014).
730 37. Winkler, E. S. *et al.* SARS-CoV-2 Causes Lung Infection without Severe Disease in Human
731 ACE2 Knock-In Mice. *J. Virol.* **96,** e0151121 (2022).
732 38. Yinda, C. K. *et al.* K18-hACE2 mice develop respiratory disease resembling severe
733 COVID-19. *PLoS Pathog.* **17,** e1009195 (2021).
734 39. Zheng, J. *et al.* COVID-19 treatments and pathogenesis including anosmia in K18-hACE2
735 mice. *Nature* **589,** 603–607 (2021).
736 40. Golden, J. W. *et al.* Human angiotensin-converting enzyme 2 transgenic mice infected with
737 SARS-CoV-2 develop severe and fatal respiratory disease. *JCI Insight* **5,** (2020).
738 41. Cadwell, K. *et al.* A key role for autophagy and the autophagy gene Atg16l1 in mouse and
739 human intestinal Paneth cells. *Nature* **456,** 259–263 (2008).
740 42. Cadwell, K. *et al.* Virus-plus-susceptibility gene interaction determines Crohn's disease
741 gene Atg16L1 phenotypes in intestine. *Cell* **141,** 1135–1145 (2010).
742 43. Matsuzawa-Ishimoto, Y. *et al.* Autophagy protein ATG16L1 prevents necroptosis in the

743 intestinal epithelium. *J. Exp. Med.* **214,** 3687–3705 (2017).
744 44. Schluter, J. *et al.* The gut microbiota is associated with immune cell dynamics in humans.
745 *Nature* **588,** 303–307 (2020).
746 45. Gopalakrishnan, V. *et al.* Gut microbiome modulates response to anti-PD-1 immunotherapy
747 in melanoma patients. *Science* **359,** 97–103 (2018).
748 46. Diefenbach, C. S. *et al.* Microbial dysbiosis is associated with aggressive histology and
749 adverse clinical outcome in B-cell non-Hodgkin lymphoma. *Blood Adv.* **5,** 1194–1198
750 (2021).
751 47. Sokol, H. *et al.* Faecalibacterium prausnitzii is an anti-inflammatory commensal bacterium
752 identified by gut microbiota analysis of Crohn disease patients. *Proc. Natl. Acad. Sci. USA*
753 **105,** 16731–16736 (2008).
754 48. Wrzosek, L. *et al.* Bacteroides thetaiotaomicron and Faecalibacterium prausnitzii influence
755 the production of mucus glycans and the development of goblet cells in the colonic
756 epithelium of a gnotobiotic model rodent. *BMC Biol.* **11,** 61 (2013).
757 49. Seibert, B. *et al.* Mild and Severe SARS-CoV-2 Infection Induces Respiratory and Intestinal
758 Microbiome Changes in the K18-hACE2 Transgenic Mouse Model. *Microbiol. Spectr.* **9,**
759 e0053621 (2021).
760 50. Sencio, V. *et al.* Alteration of the gut microbiota following SARS-CoV-2 infection
761 correlates with disease severity in hamsters. *Gut Microbes* **14,** 2018900 (2022).
762 51. Sokol, H. *et al.* SARS-CoV-2 infection in nonhuman primates alters the composition and
763 functional activity of the gut microbiota. *Gut Microbes* **13,** 1–19 (2021).
764 52. Zhang, F. *et al.* Prolonged Impairment of Short-Chain Fatty Acid and L-Isoleucine
765 Biosynthesis in Gut Microbiome in Patients With COVID-19. *Gastroenterology* **162,** 548–
766 561.e4 (2022).
767 53. Gaebler, C. *et al.* Evolution of antibody immunity to SARS-CoV-2. *Nature* **591,** 639–644
768 (2021).
769 54. Park, S.-K. *et al.* Detection of SARS-CoV-2 in Fecal Samples From Patients With
770 Asymptomatic and Mild COVID-19 in Korea. *Clin. Gastroenterol. Hepatol.* **19,** 1387–
771 1394.e2 (2021).
772 55. Xiao, F. *et al.* Evidence for Gastrointestinal Infection of SARS-CoV-2. *Gastroenterology*
773 **158,** 1831–1833.e3 (2020).
774 56. Cheung, K. S. *et al.* Gastrointestinal Manifestations of SARS-CoV-2 Infection and Virus
775 Load in Fecal Samples From a Hong Kong Cohort: Systematic Review and Meta-analysis.
776 *Gastroenterology* **159,** 81–95 (2020).
777 57. Lamers, M. M. *et al.* SARS-CoV-2 productively infects human gut enterocytes. *Science* **369,**
778 50–54 (2020).
779 58. Cao, J. *et al.* Integrated gut virome and bacteriome dynamics in COVID-19 patients. *Gut*
780 *Microbes* **13,** 1–21 (2021).
781 59. Klag, T., Stange, E. F. & Wehkamp, J. Defective antibacterial barrier in inflammatory bowel
782 disease. *Dig. Dis.* **31,** 310–316 (2013).
783 60. Ramanan, D. & Cadwell, K. Intrinsic defense mechanisms of the intestinal epithelium. *Cell*
784 *Host Microbe* **19,** 434–441 (2016).
785 61. Schluter, J. & Foster, K. R. The evolution of mutualism in gut microbiota via host epithelial
786 selection. *PLoS Biol.* **10,** e1001424 (2012).
787 62. McLoughlin, K., Schluter, J., Rakoff-Nahoum, S., Smith, A. L. & Foster, K. R. Host
788 selection of microbiota via differential adhesion. *Cell Host Microbe* **19,** 550–559 (2016).

63. Fernandez-Castañer, M. *et al.* Evaluation of B-cell function in diabetics by C-peptide determination in basal and postprandial urine. *Diabete Metab* **13,** 538–542 (1987).
64. Yu, S. *et al.* Paneth Cell-Derived Lysozyme Defines the Composition of Mucolytic Microbiota and the Inflammatory Tone of the Intestine. *Immunity* **53,** 398–416.e8 (2020).
65. Salzman, N. H. *et al.* Enteric defensins are essential regulators of intestinal microbial ecology. *Nat. Immunol.* **11,** 76–83 (2010).
66. van der Lugt, B. *et al.* Akkermansia muciniphila ameliorates the age-related decline in colonic mucus thickness and attenuates immune activation in accelerated aging Ercc1-/Δ7 mice. *Immun. Ageing* **16,** 6 (2019).
67. Wang, L. *et al.* An observational cohort study of bacterial co-infection and implications for empirical antibiotic therapy in patients presenting with COVID-19 to hospitals in North West London. *J. Antimicrob. Chemother.* **76,** 796–803 (2021).
68. Labarta-Bajo, L. *et al.* Type I IFNs and CD8 T cells increase intestinal barrier permeability after chronic viral infection. *J. Exp. Med.* **217,** (2020).
69. Karki, R. *et al.* Synergism of TNF-α and IFN-γ Triggers Inflammatory Cell Death, Tissue Damage, and Mortality in SARS-CoV-2 Infection and Cytokine Shock Syndromes. *Cell* **184,** 149–168.e17 (2021).
70. Giron, L. B. *et al.* Plasma Markers of Disrupted Gut Permeability in Severe COVID-19 Patients. *Front. Immunol.* **12,** 686240 (2021).
71. Xie, X. *et al.* An Infectious cDNA Clone of SARS-CoV-2. *Cell Host Microbe* **27,** 841–848.e3 (2020).
72. Gohl, D. M. *et al.* Systematic improvement of amplicon marker gene methods for increased accuracy in microbiome studies. *Nat. Biotechnol.* **34,** 942–949 (2016).
73. Wang, Q., Garrity, G. M., Tiedje, J. M. & Cole, J. R. Naive Bayesian classifier for rapid assignment of rRNA sequences into the new bacterial taxonomy. *Appl. Environ. Microbiol.* **73,** 5261–5267 (2007).
74. Pawlowsky-Glahn, V., Egozcue, J. J. & Tolosana-Delgado, R. *Modelling and analysis of compositional data*. (John Wiley & Sons, Ltd, 2015). doi:10.1002/9781119003144
75. Kruschke, J. K. Bayesian estimation supersedes the t test. *J. Exp. Psychol. Gen.* **142,** 573–603 (2013).
76. Homan, M. D. & Gelman, A. The No-U-Turn Sampler: Adaptively Setting Path Lengths in Hamiltonian Monte Carlo. *J. Mach. Learn. Res.* **15,** 1593–1623 (2014).

Supporting Information

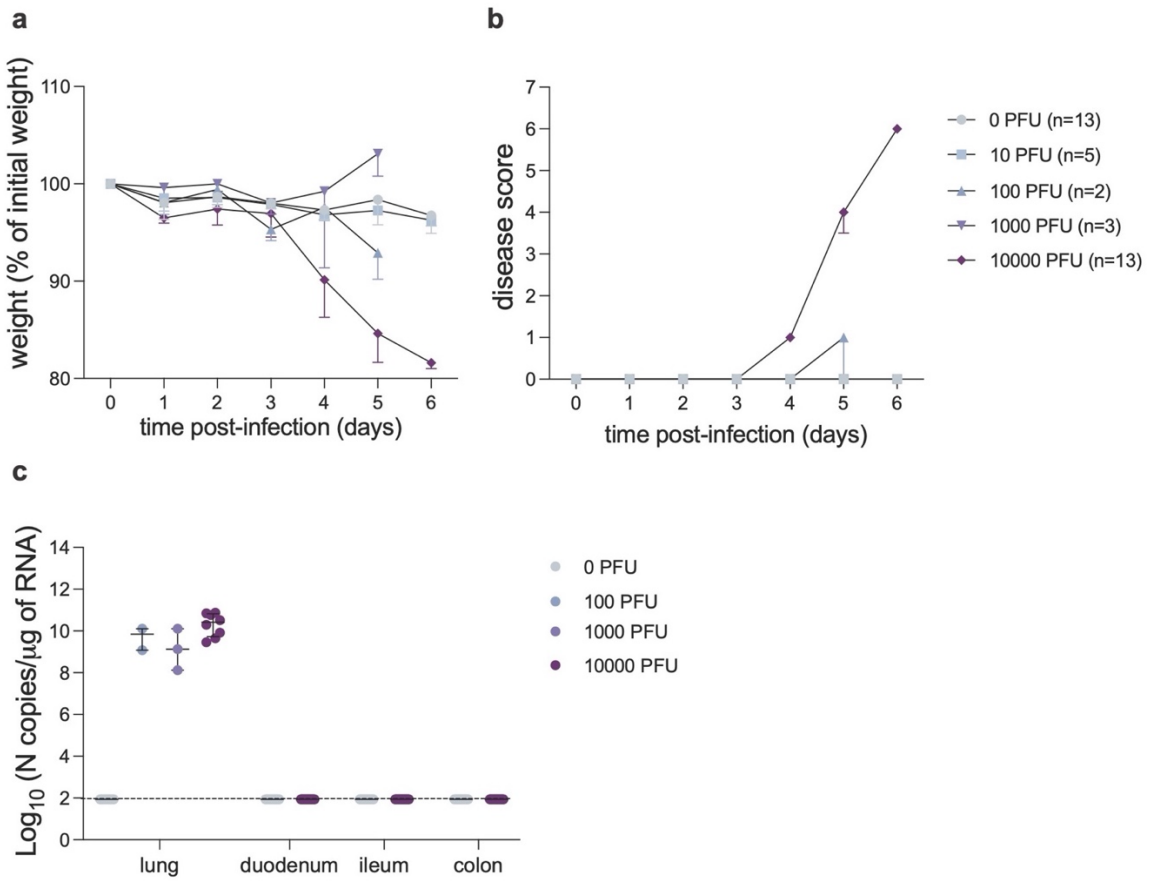

Extended Data Fig. S1 SARS-CoV-2 infection in K18-hACE2 mice.

a-b. Following inoculation with 0, 10, 100, 1000 or 10000 PFU of SARS-CoV-2 or mock infection, mice were monitored daily for weight loss (a) and signs of disease quantified by a composite score based on ruffled fur, hunched back, heavy breathing and absence of mobility (b). Median and interquartile range determined for each group at each time point are depicted. Results are pooled from 1-3 independent experiments. For each group, the total number of mice is indicated. c. Viral burden in lung or intestinal tissue of K18-hACE2 mice was analyzed at 5-6 days after infection with 100, 1000, 10000 PFU of SARS-CoV-2 or mock infection by qRT-PCR. Dots represent the copy number of N RNA per µg of RNA calculated for each mouse. Results were pooled from 1 (100 and 1000 PFU doses) or 2 (mock and 10000 PFU) independent experiments with n=2-5 mice per group for each experiment. The median and interquartile range are depicted for each experimental group. The dotted line depicts the limit of detection.

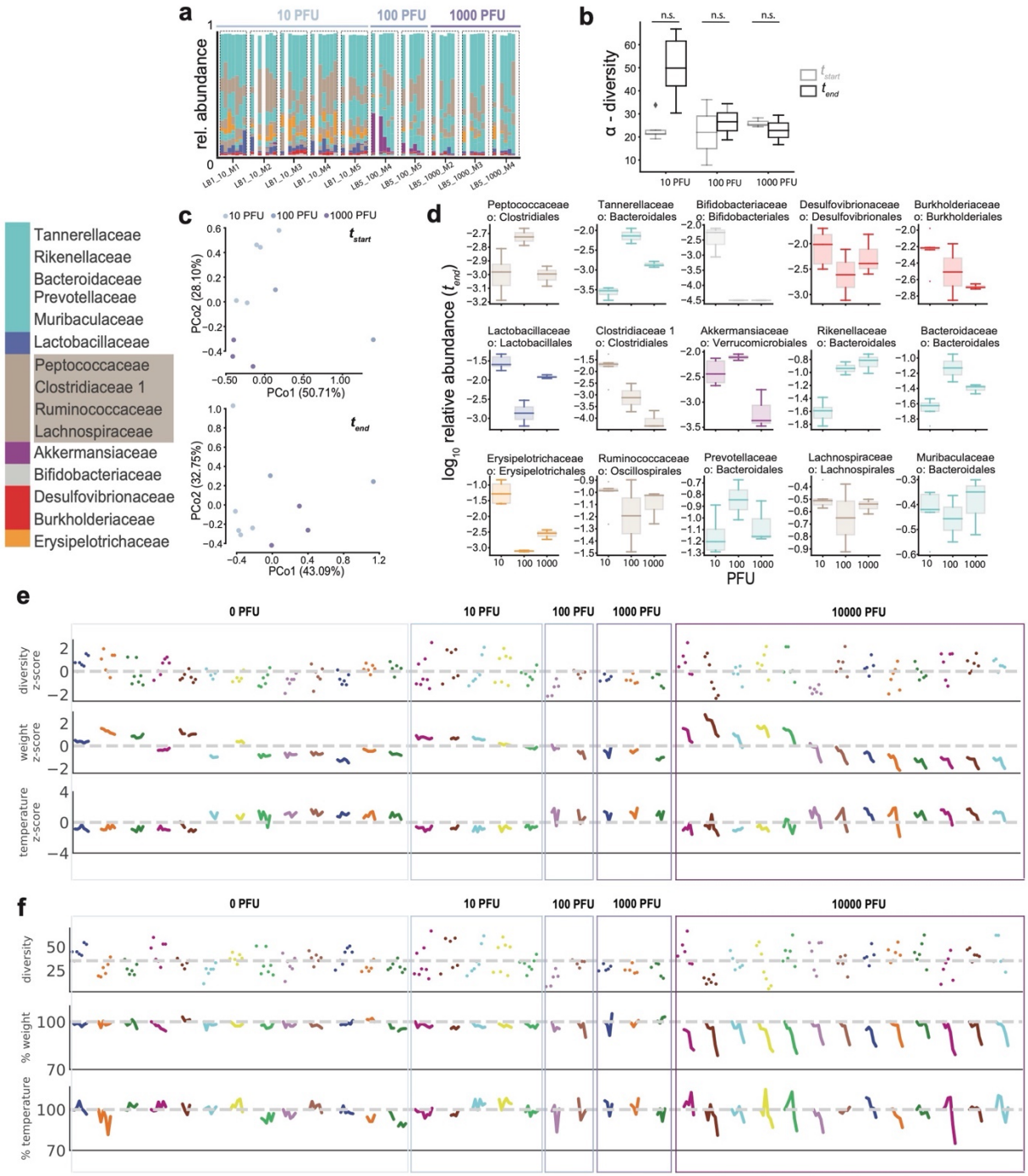

Extended Data Fig. S2 Inconsistent microbiomes dynamics in mice with lower infection doses. a Bars represent bacterial family compositions in stool samples collected from mice over time, mouse time courses grouped as indicated by boxes. **b** bacterial alpha diversity in first (t_{start})

844 and last (t_{end}) samples collected. **c** principal coordinate plots of bacterial compositions in first and
845 last samples colored by infection dose (in PFU). **d** bacterial family abundances by infection dose
846 at the final sample collected. **E** diversity, weight and temperature z-scores (calculated from all
847 data points) over time per mouse as shown in a and Fig. 1. **F** untransformed diversity, weights
848 and temperatures relative to the beginning of the experiment.
849
850

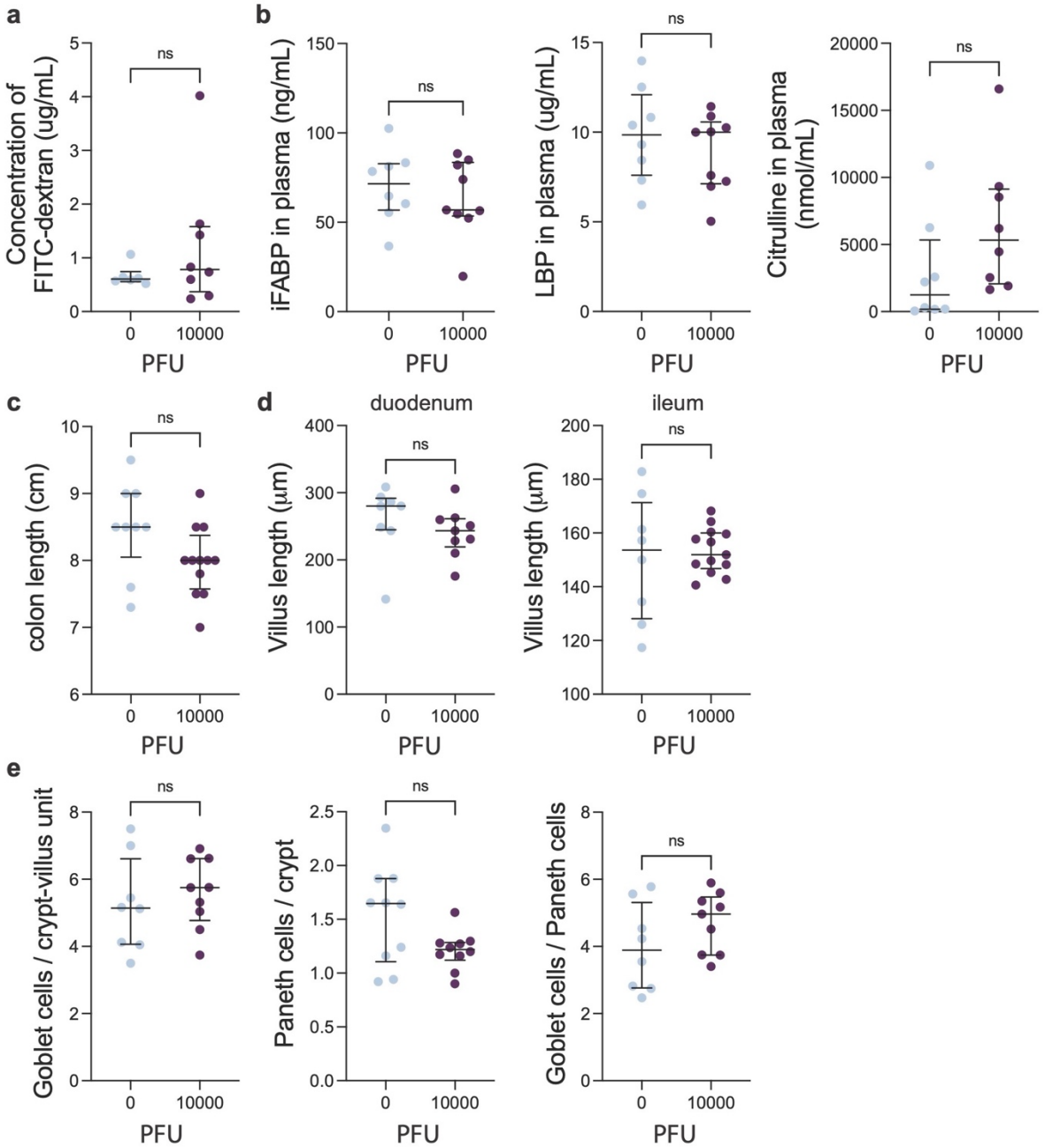

Extended Data Fig. S3 Some intestinal parameters are not modified during SARS-CoV-2 infection. K18-hACE2 mice were analyzed on day 5-6 post intranasal inoculation with 10000 PFU SARS-CoV-2 or mock treatment. **a.** Quantification of fluorescence intensity in the blood following oral administration of FITC-dextran. **B.** Intestinal fatty acid-binding protein (iFABP), LPS-binding protein (LBP), and citrulline concentration in plasma. **C.** Quantification of colon length. **d.** Quantification of villus length in the duodenum (left) and ileum (right) based on H&E staining. **E.**

859 Quantification of goblet cell number (left) and Paneth cell number (middle) per crypt-villus unit
860 in the proximal duodenum based on H&E staining and calculation of goblet cell per Paneth cell
861 ratio based on these quantifications (right). Individual mice, represented by the circles as well as
862 the median and interquartile ranges are depicted. In d, e, each circle shows the mean for each
863 mouse of the cell number counted per crypt-villus unit on 50 units. Results were pooled from 2
864 (for a) or 3 independent experiments with n=3-5 mice per group for each experiment. Significant
865 differences were determined using the Mann-Whitney U test (ns=non-significant, $p > 0.05$; **,
866 $p < 0.01$; ***, $p < 0.001$; ****, $p < 0.0001$).

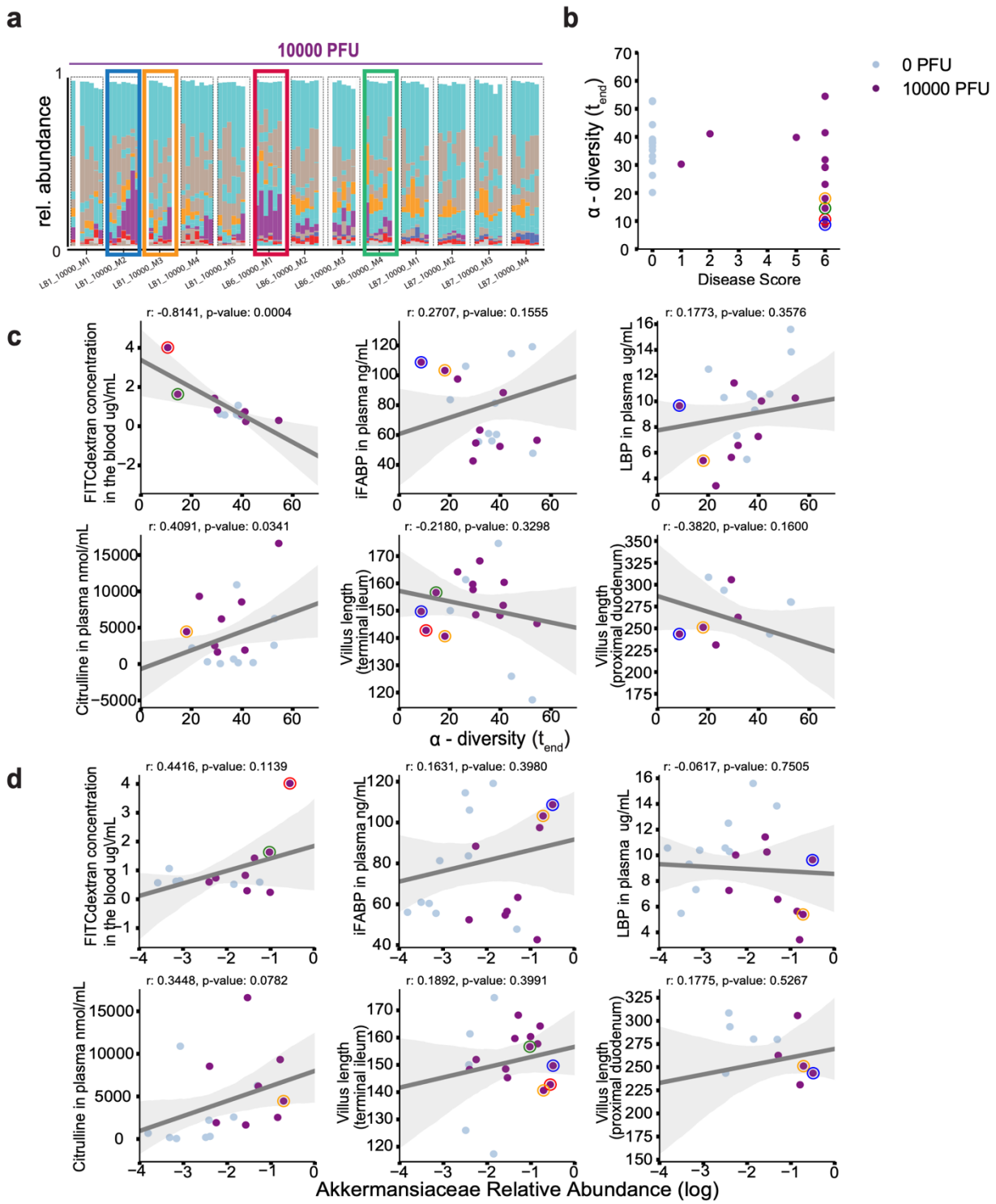

Extended Data Fig. S4 Strongest gut dysbiosis is correlated with markers of defects in the intestinal barrier and epithelium. A Reproduction of Fig. 1 showing bacterial compositions in mice infected with 10^4 PFUs, highlighting four mice time courses of mice with lowest diversity

872 and highest disease scores at the end of the experiment (**b**). **c-d** Correlations between alpha
873 diversity (**c)** (inverse Simpson) and $\log_{10}$ relative *Akkermansia* abundances (**d**) at the end of the
874 experiment with epithelium phenotypes and gut barrier integrity markers measured in the blood
875 of mice (data from mice highlighted in **a** with circles in corresponding colors, lines: linear
876 regression, shaded region: 95%CI).
877
878

879

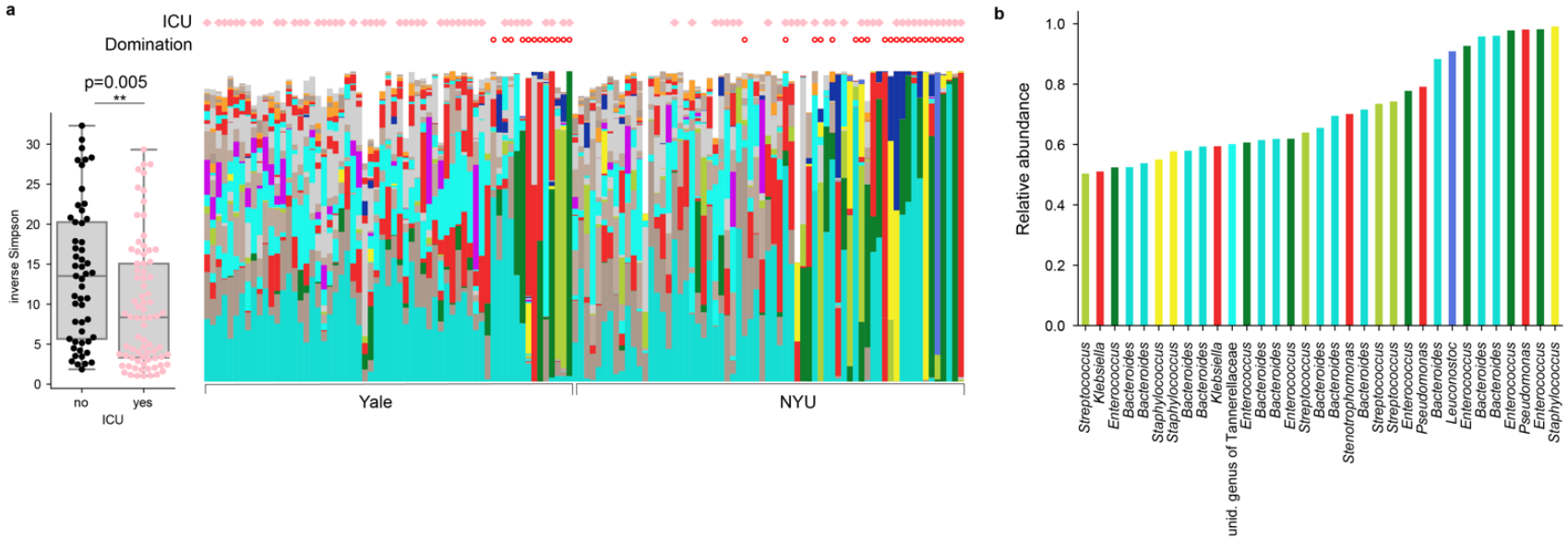

880

881 **Extended Data Fig. S5 a** Samples from patients requiring ICU transfer have lower diversity on average (p=0.005, Wilcoxon rank-
882 sum); bars as in Fig. 1 with ICU status of patients and domination state of samples indicated. **b** Genus abundances in samples with a
883 single genus >50% relative abundance.

884

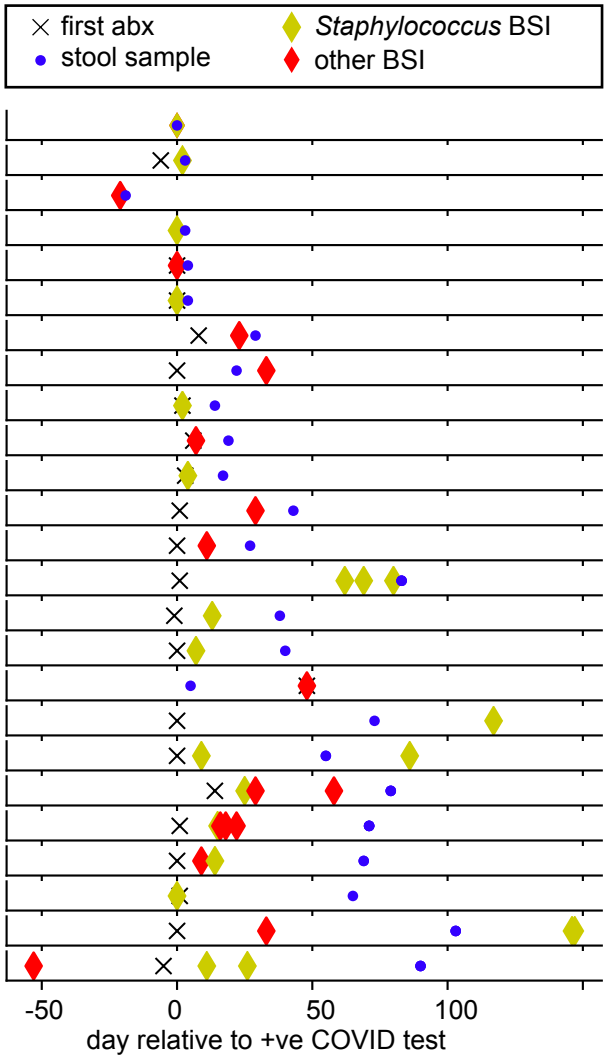

885

886 **Extended Data Fig. S6** Patients with a positive clinical blood culture result (BSI) received
887 antibiotics, prior or on the day of blood culture results (cross symbol: first recorded antibiotic
888 administration, blue: sequenced stool sample, diamond: positive blood culture result (BSI)).
889

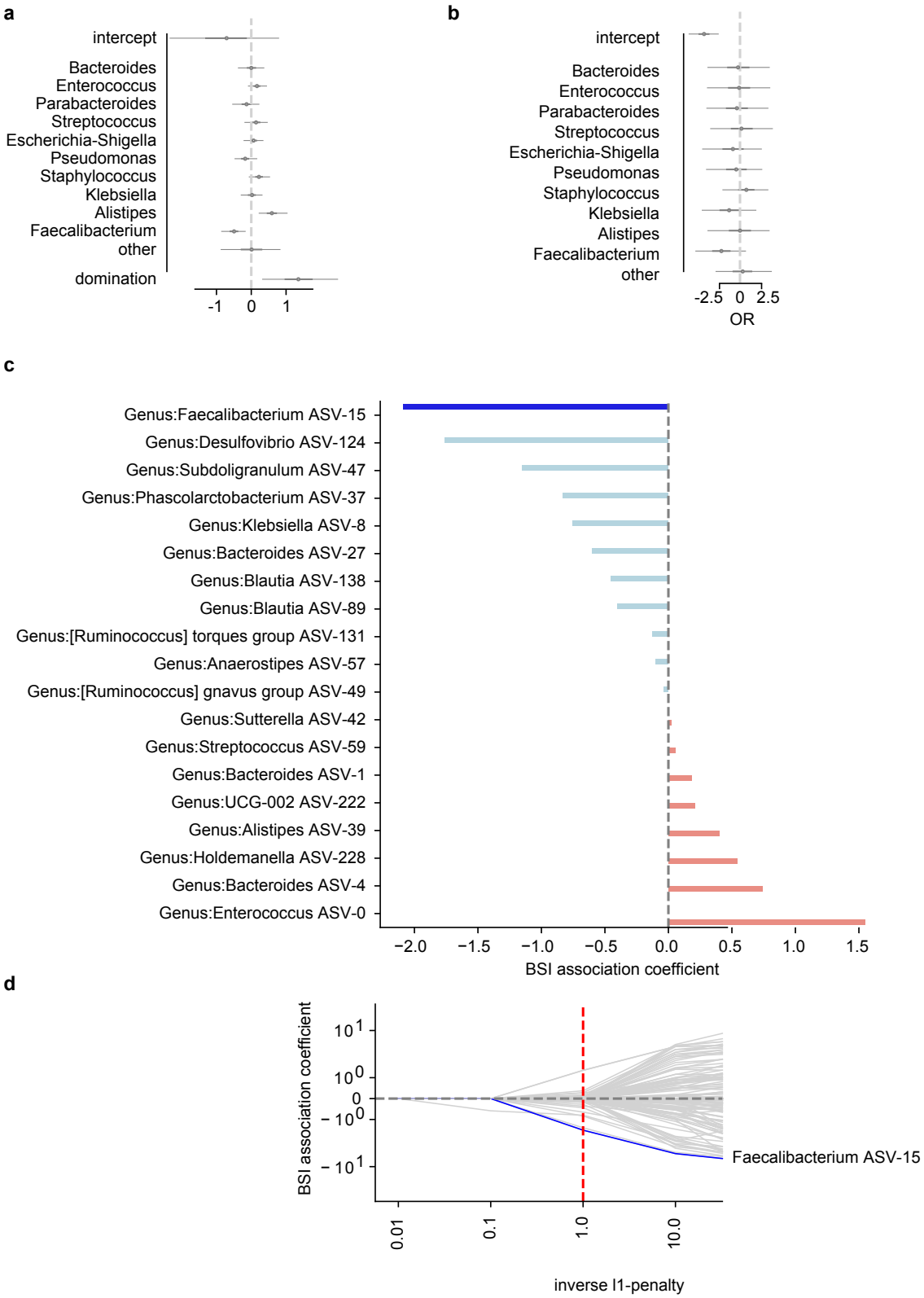

890

891 **Extended Data Fig. S7 a** Posterior coefficient estimates from a Bayesian logistic regression

892 regressing $\log_{10}$ relative abundances of the top 10 most abundant bacterial genera on BSI status

using only BSI cases with associated stool samples taken prior or on the day of a confirmed positive blood culture. **b** Posterior coefficient estimates from a Bayesian logistic regression regressing $\log_{10}$ relative abundances of the top 10 most abundant bacterial genera on BSI status with domination status of the microbiome as an additional predictor (domination: >50% of the composition by one taxon). **c** ASVs associated with samples from patients with BSI. Coefficients from a cross-validated, L1-penalized logistic regression correlating the binary outcome (BSI) with $\log_{10}$-transformed relative ASV abundances. **d** Cross-validation paths; for all regularization strengths (L1-penalty) used, a *Faecalibacterium* ASV was most negatively associated with BSI-positive samples.

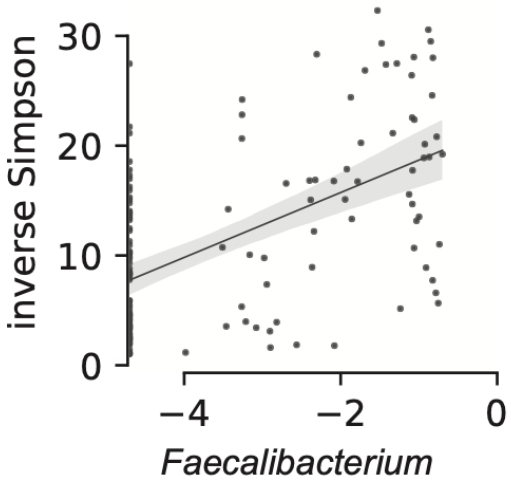

Extended Data Fig. S8 *Faecalibacterium* relative abundance is positively correlated with bacterial alpha diversity. Log10 transformed relative abundances of the genus *Faecalibacterium* in stool samples from patients are correlated with the inverse Simpson diversity index; line from linear regression, shaded region: 95%CI.

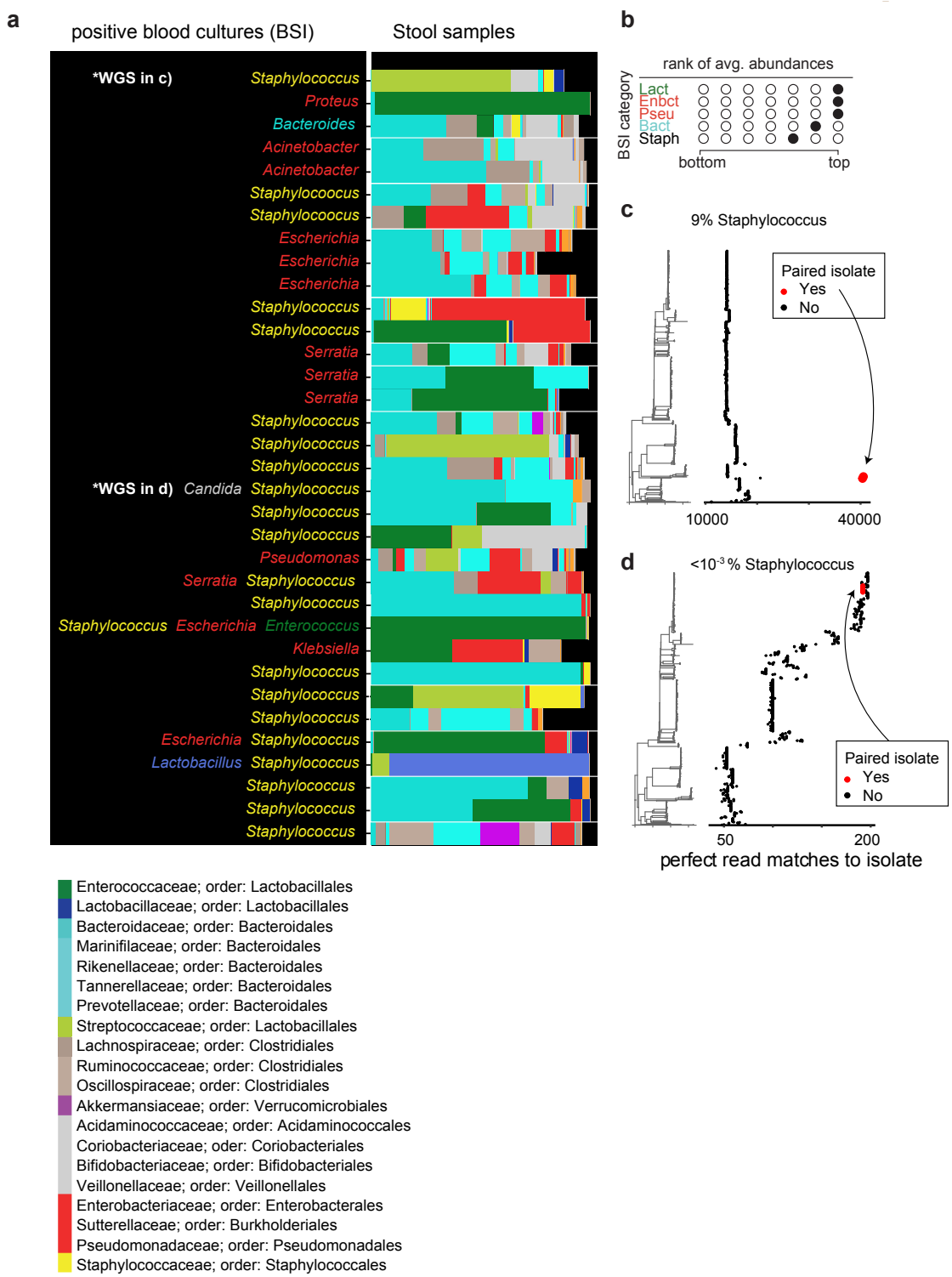

Extended Data Fig. S9 Bacteria in stool of COVID-19 patients match taxa identified blood cultures. a Organisms identified in blood cultures together with bars representing the bacterial

911 family compositions in stool samples; multiple samples belonging to the same patient grouped
912 by a white box. Two samples with matching whole genome sequenced (WGS) blood isolates
913 indicated. **b** Rank analysis of abundance patterns in stool samples from different BSI categories;
914 a filled circle indicates the calculated rank of the focal BSI category (row) in terms of the
915 corresponding taxon stool abundance relative to samples from other BSI categories (Lact:
916 Lactobacillales, Enbct: Enterobacterales; Pseu: Pseudomonadales, Bact: Bacteroidales, Staph:
917 Staphylococcales. Only 5 out of 7 BSI categories are shown because fungal BSIs and the
918 uninfected category have no corresponding bacterial stool abundances). **c,d** left: neighbor-joining
919 tree constructed from all NCBI RefSeq assemblies of *Staphylococcus aureus* genomes in
920 addition to isolates that were isolated from subjects highlighted in **a**. right: counts of perfect read
921 matches of shotgun metagenomic reads from stool samples, red: stool sample sequencing read
922 matches to WGS of isolates from the same patient, black: matches to other genomes.

923 **Supplementary Table 1: Clinical characteristics of patients with confirmed COVID-19 at**
924 **NYU Langone Health and Yale New Haven Hospital**
925

	NYU, N = 60	**YALE, N = 36** 926
Age (years)	51 ± 17.5	62.52 ± 19.72
Sex (F | M)	42% | 58%	39% | 61%
Hospital course and Outcomes		
ICU Admission	53%	65%
Pneumonia	42%	77%
Diarrhea	13%	32%
Intubation	36%	41%
Sepsis	23%	18%
Encephalopathy	12%	3%
Death	5%	21%
Length of stay (median, IQR)	37 (10-86)	27 (11-35.25)
Risk Factors		
Cancer within 1 year	7%	4%
Chronic Heart Disease	18%	36%
Hypertension	38%	64%
Chronic Lung Disease	7%	20%
Immunosuppression	17%	4%

927 **Supplementary Table 2: Clinical characteristics of COVID-19 patients at NYU Langone**
928 **Health and Yale New Haven Hospital with and without positive blood culture results (BSI).**
929

	BSI, N = 26	non-BSI N = 53
Hospital course and Outcomes		
ICU Admission	69%	64%
Pneumonia	73%	53%
Diarrhea	31%	64%
Intubation	58%	36%
Sepsis	35%	21%
Encephalopathy	19%	6%
Death	15%	9%
Length of stay (median, IQR)	59 (23-91.5)	22 (6-51)

930
931
932

933 **Supplementary Table 3: Shotgun metagenomic reads mapped to species identified in clinical blood cultures**. Dark grey shading:
934 no sequencing reads from stool samples matched the species identified in clinical blood samples, light grey shading: species of the
935 same genus but not the same species had non-zero read counts in stool samples. The relative abundance of identified species were
936 contrasted with their mean abundances (log10 ratio).
937

Organism identified in blood	species identified in stool sample	Log ratio
Bacteroides thetaiotaomicron	Bacteroides_thetaiotaomicron_14-106904-2	2.92
Enterococcus faecalis Group D	Enterococcus_faecalis_LD33	1.8
Escherichia coli	Escherichia_coli_K-12_substr._W3110	2.2
Escherichia coli	Escherichia_coli_IAI39	1.6
Escherichia coli	Escherichia_coli_536	2.8
Klebsiella pneumoniae	Klebsiella_pneumoniae_KPNIH27	-1.7
Lactobacillus species	Lactobacillus_curvatus_WiKim38	3.9
Pseudomonas aeruginosa	Pseudomonas_aeruginosa_SJTD-1	3.3
Serratia marcescens	Serratia_marcescens_CAV1492	-0.2
Staphylococcus aureus	Staphylococcus_aureus_RF122	1.9
Proteus mirabilis	Proteus_mirabilis;t__Proteus_mirabilis_BB2000	0.56
Acinetobacter lwolfii	Acinetobacter_calcoaceticus_EGD_AQ_BF14	-0.6
Staphylococcus	Staphylococcus_sp._HMSC063G01_HMSC063G01	0.9
Staphylococcus	Staphylococcus_epidermidis_W23144	3.3
Staphylococcus aureus	not found	
Staphylococcus hominis	not found	
Staphylococcus capitis	not found	
Staphylococcus epidermidis, hominis	Staphylococcus_pseudintermedius_063228	2.2
Staphylococcus epidermidis, hominis ssp hominis	not found	
Staphylococcus epidermidis	Staphylococcus_aureus_JKD6008	2.7
Staphylococcus epidermidis	Staphylococcus_epidermidis_DAR1907	1.1
Staphylococcus capitis	Staphylococcus_sp._HMSC067F07_HMSC067F07	3.7
Staphylococcus epidermidis, hominis ssp hominis	Staphylococcus_hominis_793_SHAE	0.8
Staphylococcus epidermidis	Staphylococcus_sp._HMSC070D05_HMSC070D05	3.8
Staphylococcus hominis, epidermidis	Staphylococcus_hominis_MMP2	1.0
Staphylococcus hominis, epidermidis	Staphylococcus_epidermidis_ATCC12228 GCF7645.1	0.2

938

939 **Supplementary Table 4:** SRA accession numbers for the bioproject PRJNA745367
940 corresponding to the mouse sequencing data.
941 (Excel sheet)
942
943 **Supplementary Table 5**: SRA accession numbers for the bioproject PRJNA746322
944 corresponding to the human stool samples sequencing data.
945 (Excel sheet)
946